REPORT
doi:10.26443/seismica.v4i2.1482

First DAS observations from the GeoLab fibre in Madeira, Portugal

Afonso Loureiro * [1,2], **David Schlaphorst** [2], **Luís Matias** [2], **Andreia Pereira** [2], **Carlos Corela** [2], **Susana Gonçalves** [2], **Rui Caldeira** [1]

[1]Agência Regional para o Desenvolvimento da Investigação, Tecnologia e Inovação, Funchal, Portugal, [2]IDL - Instituto Dom Luiz, Faculdade de Ciências, Universidade de Lisboa, 1749-016 Lisboa, Portugal

Author contributions: *Conceptualization*: Afonso Loureiro. *Software*: Afonso Loureiro, David Schlaphorst, Susana Gonçalves. *Formal Analysis*: Afonso Loureiro, David Schlaphorst, Andreia Pereira, Luís Matias, Carlos Corela. *Writing - Original draft*: Afonso Loureiro. *Writing - Review & Editing*: Afonso Loureiro, David Schlaphorst, Andreia Pereira, Susana Gonçalves. *Funding acquisition*: Luís Matias, Rui Caldeira.

Abstract Distributed Acoustic Sensing allows extremely dense acquisition geometries of strain data. The GeoLab fibre, installed on the southern coast of Madeira Island, extends for ∼56 km and is exclusively dedicated to research. This fibre provides an invaluable resource for continuous data collection and analysis. Between October 26th and November 3rd, 2023, ∼7 TB of data were collected at 500 Hz with gauge length of 10.2 m at each 5.1 m. This report highlights the versatility of the GeoLab fibre and the present dataset for seismological, oceanographic, and biological research with a non-exhaustive collection of examples in various scientific domains, such as local and teleseismic events, calls from different species of baleen whales, waves and their interaction with the shoreline, ocean-bottom currents and temperatures, and anthropogenic noise sources.

Non-technical summary Distributed Acoustic Sensing allows the collection of detailed strain data with extremely fine spatial and temporal resolution. The GeoLab fibre, installed on the southern coast of Madeira Island, stretches for ∼56 km and is dedicated solely to research. From October 26th to November 3rd, 2023, ∼7 TB of data were collected at a rate of 500 samples per second, with data points each 5.1 m. We collected data for, among others, local and distant earthquakes, fin, blue and sei whale calls, car and ship traffic, and ocean waves. With a collection of examples, this report demonstrates the versatility of the dataset for research in various scientific fields.

Production Editor:
Andrea Llenos
Handling Editor:
Wenbo Wu
Copy & Layout Editor:
Hannah F. Mark

Received:
October 7, 2024
Accepted:
October 21, 2025
Published:
December 13, 2025

1 Introduction

GeoLab is an initiative aimed at the research community with the participation of Fundação para a Ciência e Tecnologia (FCT), Fundação para a Computação Científica Nacional (FCCN), Agência Regional para o Desenvolvimento da Investigação, Tecnologia e Inovação (ARDITI), EllaLink, EMACOM and GÉANT. As part of GeoLab, a single dark optic fibre on the Madeira branch of EllaLink (Fig. 1) is made available for research in seismology, oceanography, and biology.

Within the scope of Oceanic Observatory of Madeira (OOM), the GeoLab fibre will enable a more comprehensive characterization of the Madeira Basin when used in conjunction with other observational capabilities. By integrating DAS with data from surface and satellite observations, moorings, gliders, and other autonomous underwater platforms, it will be possible to study various oceanographic and biological parameters throughout the water column. Furthermore, the fibre will function as a permanent acoustic monitoring station, offering insights into the ocean's soundscape. This will aid in identifying both anthropogenic and natural sources of underwater noise. The high density of sensing channels enabled by DAS will also allow a detailed study of local and regional seismicity and imaging of the crustal structure beneath the fibre, contributing to a holistic understanding of the geological, geophysical, and environmental dynamics of the basin.

The current dataset has been acquired to showcase the sensitivity and potential of the GeoLab fibre in detecting a range of environmental and geophysical parameters. It is intended as an open resource for the research community, supporting further exploration, validation, and innovation across disciplines such as seismology, oceanography, and marine biology. This dataset will facilitate collaborative efforts and drive advancements in our understanding of the Madeira Basin and similar marine environments.

1.1 Optical fibres as distributed sensors

Optical fibres are used for communication, but can also be used as distributed sensors to derive measurements of different physical properties by analysing the back-scattering of laser light pulses as they travel along the fibre. The position of the scattering elements is determined by the two-way travel time of each light pulse and its back-scattering.

Linear strain, pressure, and temperature induce

*Corresponding author: maloureiro@fc.ul.pt

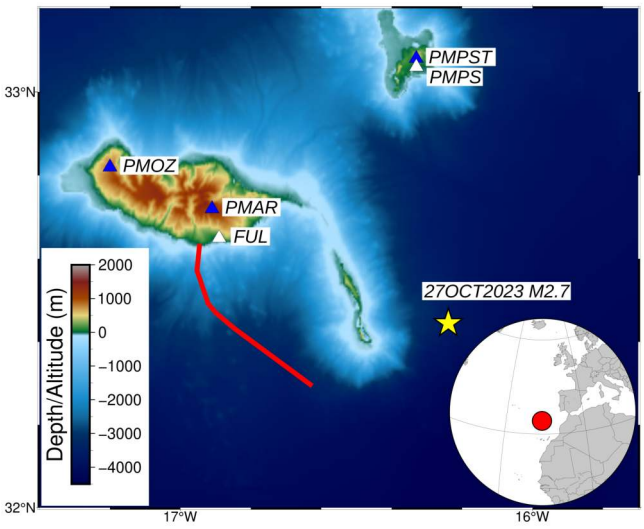

Figure 1 Map of the Madeira archipelago, showing locations of the cable and permanent seismic stations. Red line: approximate location of the GeoLab fibre. Blue triangles: permanent broadband seismic stations. White triangles: permanent short-period seismic stations. Yellow star: local earthquake recorded during the data acquisition period. Topography and bathymetry source: GEBCO Compilation Group (2023).

changes in the refractive index of the fibre, affecting not only the propagation of light along the fibre, but also how the energy that is back-scattered by different processes (Hocker, 1979; Hamza et al., 2004; Seabrook et al., 2022; Peláez Quiñones et al., 2023; Becerril et al., 2024).

Most of the backscattered light is due to elastic Rayleigh scattering, without experiencing wavelength changes (Palmieri, 2013). This scattering process is used by DAS to characterise the acoustic field in terms of amplitude, wavelength and phase over a wide dynamic range (Lindsey et al., 2020).

1.1.1 Distributed Acoustic Sensing

DAS is a technique that enables the precise measurement of broadband strain with extremely high spatial and temporal resolution. The first usages of optical fibres for strain sensing date back to the 1970s (Bucaro et al., 1977; Cole et al., 1977). Measuring the fringe pattern of the Rayleigh backscattering was first proposed in 1992 (Juškaitis et al., 1992; Juškaitis et al., 1994), initially to measure temperatures (Rathod et al., 1994), and later also to measure strain (Froggatt and Moore, 1998). For research, the technique has gained considerable traction since 2005 (Hartog, 2017).

The strain or strain rate wavefield is inferred from phase and amplitude variations of coherent Rayleigh back-scattering of light pulses travelling along the optical fibre. If only the amplitude of the back-scattering is used, the DAS interrogator behaves as an optical time-domain reflectometer (OTDR), where the precise location of the scatterers is determined by time-gating the reflected light pulse.

These phase variations occur primarily due to extensional and contractional strain altering the transmission properties of optical fibres. Still, temperature fluctuations also affect the optical properties of the glass medium and lower refractive index cladding (Yeung and Johnston, 1978; Hamza et al., 2004, for example). Although the fibre itself has low sensitivity to pressure waves, coating and cladding increase this sensitivity (Hartog, 2017), as the coating spreads laterally instead of contracting, inducing strain on the fibre (Bucaro et al., 1977).

The minimum sampling distance, or instrument channel, is the length of fibre required to guarantee that a signal is distinguishable from background noise, and it depends on the sensitivity of the detector and the precision of the timing circuits. The width of the laser pulse is set to this minimum distance (Capdeville and Sladen, 2024). It is essential to note that the amplitude of the signal recorded at each channel is obtained through the coherent addition of many Rayleigh scatterers with random phases and amplitudes, originating from the optical non-linearities of the fibre itself (Toulouse, 2005). This results in a non-linear dependence on the external signal (Gabai and Eyal, 2016). The same imperfections of the optic fibres that DAS explores also cause light attenuation (Blanc et al., 2022; Kislov and Gravirov, 2022), which limits detection range, either due to the back-scattered energy falling below the detection threshold of the interrogator or due to the outgoing light pulses reaching a repeater. Repeaters are needed on fibres used for communications to boost the attenuated signal.

To improve the signal-to-noise ratio (SNR), measurements can be integrated over space and time. Over time, the interrogator itself stacks consecutive measurements at a frequency higher than the nominal sampling rate (Capdeville and Sladen, 2024). Over space, multiple instrument channels are generally combined into the effective measurement distance, termed G_L. Longer gauge lengths improve the SNR, but the averaging along an increasing number of instrument channels also introduces a low-pass filter (Dean et al., 2016; Martin et al., 2021). The data stream from each G_L is also commonly referred to as a channel, similarly to how data from conventional seismic instruments is described. Unless otherwise specified, G_L and channel will be used interchangeably throughout this report.

The maximum sampling frequency is limited by the length of the fibre, which directly affects the two-way time of the light pulses (Lindsey and Martin, 2021), as a new pulse can only be transmitted after the back-scattered light from the previous pulse is received. The internal oversampling to increase the SNR reduces the maximum achievable sampling rate.

1.2 Instrumental response

Assuming sufficiently small displacements, the amplitude and phase response of broadband seismometers to ground motion is well established and can be expressed as:

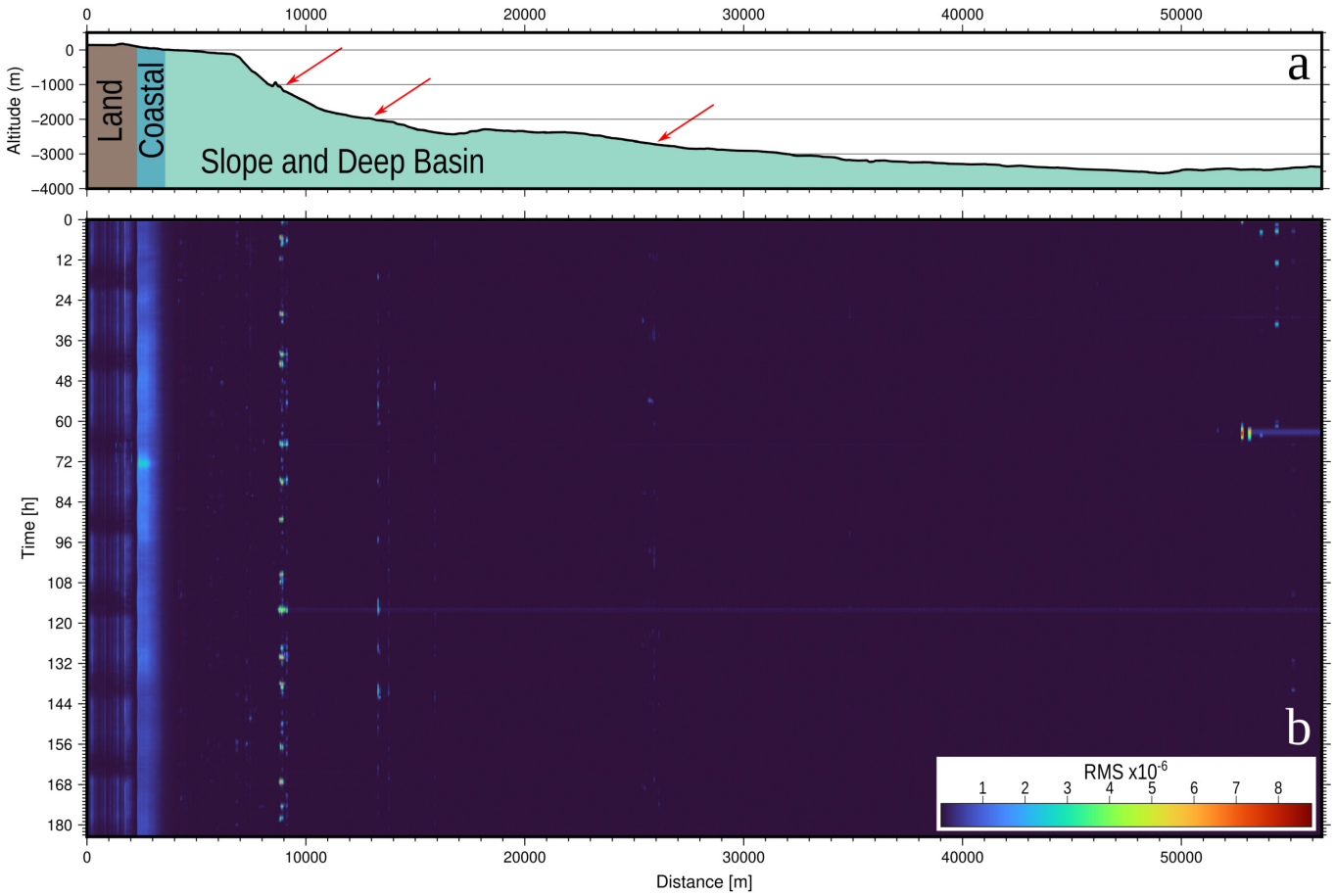

Figure 2 Global RMS map. a) Depth profile for the GeoLab fibre, extracted from GEBCO Compilation Group (2023). Colours indicate the three different data domains: 1) from 0 km to ∼2 km, segment of the cable on land; 2) from ∼2 km to ∼3 km, narrow shelf where ocean waves dominate the spectrum; 3) island slope and deep basin from ∼3 km to the end of the fibre. Red arrows indicate suspected free-hanging sections of the cable at ∼9 km, ∼13 km and ∼26 km. b) Global RMS map for the entire dataset, calculated in 30 min windows for each G_L. Major crosstalk events occur at 116 h (∼9 km) and 63 h (∼53 km).

$$u_i(x,\omega) = \sum_{j=1}^{3} T_{ij}(\omega) g_j(x,\omega) \quad . \tag{1}$$

The i$^{\text{th}}$ component of the observed displacement $u_i(x,\omega)$, at location x and for angular frequency ω, is a function of the true ground deformation $g(x,\omega)$ and a linear transfer function $T(\omega)$, in which j is the component of ground deformation in a suitable orthogonal coordinate system.

Ideally, equivalent transfer functions should be derived for DAS deployments, as the deformation of the surrounding medium causes changes in measured strain or strain rate. However, because optical fibre can only provide measurements along the cable direction, or the unit vector $\mathbf{e}(\mathbf{x})$, a scalar approximation is required (Paitz et al., 2020):

$$u_e(x,\omega) = T_e(\omega) g_e(x,\omega) + J \quad , \tag{2}$$

where u_e and g_e are the projections of u and g along the fibre direction. J encompasses several other factors pertaining only to the fibre and not present on traditional seismometers, such as sensitivity to different physical phenomena besides ground motion (Hartog, 2017) or incomplete knowledge of the fibre's optical properties. It is assumed that fibre drift, i.e., the cumulative changes in optical properties concerning the fibre's scattering locations and density variations, is negligible, even with temperature and strain oscillations (Zumberge et al., 2018; Lindsey et al., 2020). Apart from Distributed Temperature Sensing (DTS) methods, temperature variations that affect the scattering characteristics of the fibre (Zumberge et al., 2018) are also typically ignored, as they are difficult to correct without the use of additional instruments or the deployment of fibre pairs with different thermal coefficients. Furthermore, temperature changes on a seafloor cable are expected to have very low-frequency variations (Ide et al., 2021; Fernandez-Ruiz et al., 2022; Peláez Quiñones et al., 2023). The most challenging issue is the imperfect and, sometimes, variable coupling of the fibre to the ground. On sea deployments, the level of burial in the sediments, or the construction of the cables themselves, including shielding, armouring, gel filling, and the twisting of the multiple fibres (Kislov and Gravirov, 2022; Sladen et al., 2019; Fernández-Ruiz et al., 2020; Celli et al., 2023) represent other variables that directly affect how ground motion is converted into strain.

Further complicating the determination of a transfer function is the azimuthal sensitivity of DAS and associated wavenumber filtering that introduces G_L-dependent notches in the wavenumber response

(Hartog, 2017; Paitz et al., 2020). The averaged strain along the entire G_L is significantly different from the actual strain if the incident wave arrives at an angle, and different wavenumbers also translate into different measured strains. At a single point, DAS can only measure longitudinal strain, and the sensitivity drops as $cos^2\theta$, where θ is the incidence angle of plane waves. Moreover, this dependency does not hold for incidence angles close to orthogonal (Mateeva et al., 2014; Kuvshinov, 2015), and it differs for P, S, and pressure waves (Bucaro et al., 1977; Budiansky et al., 1979; Martin et al., 2021; Becerril et al., 2024). Experimental data shows a decrease in sensitivity at very shallow incidence angles (sub-parallel to the fibre), attributed to the spatial averaging along each gauge length (Potter et al., 2024). Furthermore, the interaction between different wavelengths and the gauge length causes the fibre's sensitivity to depend on both frequency and incidence angle, with the fibre responding most strongly at specific angles for a given frequency.

Polarities obtained from optical measurements are comparable to those of omnidirectional hydrophones, but the angular response is more akin to those of geophones or accelerometers, causing the response of a DAS system to be very different from conventional sensors (Hartog, 2017), with highly complex directional sensitivity that depends on wavenumber as well as the angle of incidence (Dean et al., 2015).

The apparent strain ε_{ap} measured by DAS is thus a function of the real strain on the fibre ε, the fibre's azimuthal sensitivity $g(\theta, G_L)$, the varying coupling of the fibre $f(l,t)$ in both space l and time t, the changes in the optical properties of the fibre due to ageing $h(t)$, and the thermal expansion α and thermal response β coefficients of the fibre for a given temperature variation ΔT:

$$\varepsilon_{ap} = g(\theta, G_L) f(l,t) h(t) \varepsilon + \alpha\beta\Delta T \quad . \tag{3}$$

In the near-field, the broadside sensitivity of the fibre $g(\theta, G_L)$ to plane waves is also a function of the length of the G_L used, as longer gauge lengths will detect a strain variation even if the incidence angle is 90° at the centre of the G_L. Combining all these effects means that even for short inter-channel distances, coherence might be lost (van den Ende and Ampuero, 2021).

When compared to seismometers, DAS has a lower SNR, variable angular sensitivity and an undetermined response that affects the reliability of the recorded waveforms and amplitudes. However, these drawbacks are mitigated by the extremely dense network of sensors DAS provides (Martin et al., 2021; Benjumea et al., 2024). To date, outside controlled laboratory experiments (Papp et al., 2016, for example), no transfer functions have been derived to convert strain or strain-rate measurements into ground motion. Previous attempts to obtain an approximate scalar instrument response for specific sections of fibres have relied on co-located seismometers, geophones, or hydrophones and were focused on subsets of arrivals (Daley et al., 2015; Lindsey et al., 2020; Paitz et al., 2020; Lior et al., 2021; van den Ende and Ampuero, 2021; Janneh et al., 2023; Trabattoni et al., 2023), by using Fast Discrete Curvelet Transforms to convert the strain rate into particle motions (Yang et al., 2021), or by coda calibration from empirical Green's function (EGF) (Gök et al., 2024). From the analysis of earthquake arrivals, we can already make a general qualitative characterisation of the fibre coupling (see Section 2.2.1).

2 Dataset

The GeoLab fibre (Fig. 1) starts at the Cable Landing Station of Praia Formosa and extends for ∼56 km. It is exclusively dedicated to scientific research purposes, not interfering with regular commercial traffic on the remaining fibre pairs in the same cable. It is currently instrumented with an ASN OptoDAS interrogator (Waagaard et al., 2021), capable of measuring optical phase modulation over distances exceeding 125 km, with a fixed channel spacing of 1.02 m, using frequency-modulated pulses. The interrogator uses a laser with a wavelength of 1536.61 nm (channel ITU 51). For the length of the GeoLab fibre, the system can achieve a sampling rate up to 1600 Hz. This equipment is managed by ARDITI.

As the GeoLab fibre is part of an active commercial communications infrastructure, precise cable coordinates are confidential and available only through protocols established by the end users and the consortium. The coordinates used to create the figures in this report were obtained from public documents and official cartography sources, and are generally within 200 m of the true cable position. The maximum offset is ∼1.7 km. Additionally, there are no controlled-source tests to establish the exact location of a channel or groups of channels along the fibre, nor will they be provided outside non-disclosure protocols. Degraded coordinates with a precision of approximately ∼200 m will be made available with the dataset.

2.1 Acquisition parameters

Between October 26th and November 3rd 2023, the interrogator continuously recorded phase rates with a G_L of 10.2 m (corresponding to the average phase rate over 10 consecutive instrument channels), and 5.1 m spacing (50 % superposition), for a total of 11380 channels, of which 11294 are usable. The last G_Ls correspond to positions beyond the end of the fibre. Phase rate measurements are linearly proportional to apparent strain rates (Hartog, 2017; Trabattoni et al., 2023). To obtain accurate strain rate estimates, the measurements require correction for the optical properties of the fibre and the spatial averaging effects introduced by the finite gauge length. The interrogator computes the phase difference between two backscatter locations separated by the G_L according to:

$$\Delta\dot{\varphi}(s,t) = K \cdot G_L \cdot \dot{\varepsilon}(s,t) \quad , \tag{4}$$

where (s,t) denotes the spatial position and time, G_L is the gauge length, and $\dot{\varepsilon}(s,t)$ is the observed strain rate at a given time and position along the fibre. The proportionality constant K represents the phase sensitivity of the system and is defined as:

$$K = \frac{4\pi \cdot n \cdot \xi}{\lambda} \quad , \tag{5}$$

where n is the effective refractive index of the fibre, λ is the wavelength of the laser, ξ is the fibre photoelastic effect parameter, equal to approximately 0.78 (Bertholds and Dandliker, 1988). For this acquisition, a default refractive index of $n = 1.4677$ was assumed. The corresponding sensitivity value, K, is recorded in the header groups of the data files.

We used a sweep length of 50 µs, which results in a maximum possible sampling rate is 1600 Hz for the length of the GeoLab fibre. However, data was collected at 500 Hz to reduce the amount of disk space required. This sampling frequency ensures signal fidelity up to 250 Hz, covering all the frequency bands of interest for the envisaged seismological, oceanographic and biological research objectives of ARDITI and the OOM.

To ensure that the entire available fibre was utilised, data was recorded beyond the expected end of the fibre. The last 86 channels of the dataset did not record any directly back-scattered light, but rather multi-path back-scattered energy and reflections of the outgoing laser pulses as they reach the end of the fibre.

For this dataset, the interrogator was not synchronised to UTC, as neither GPS nor NTP were available. The internal oscillators of the interrogator thus limit timing accuracy. From the comparison between the predicted and observed arrival times of S waves from several teleseismic events (Tab. S1), the DAS times are estimated to be ~150 s behind UTC (see Fig. 10). Presently, no further time corrections are available.

The fibre can be roughly divided into three domains (see Fig. 2a), each with different data characteristics. The first ~450 channels (~2300 m) correspond to the portion of the fibre between the landing station and the shore, where anthropic sources dominate. In this section, the cable runs from the interrogator to the landing station entrance as a single fibre with a standard plastic outer jacket. From the landing station to the shoreline, it runs in buried conduits, within a stainless-steel jacket, unshielded but inside a gel-filled coating (see Fig. S3).

Between the shore and channel ~800, the cable is on a narrow shelf with a water depth below 100 m, and ocean waves dominate the recording. The exact boundary between the land and oceanic domains depends on the tidal cycle (Fig. 3). The first part of this section of the cable is also trenched (~600 m) and armoured, which alters the response function of the fibre. The cable operator has not disclosed the extent of the armoured section. Then the cable runs down the island slope into the abyssal plain section, up to a maximum depth of ~3500 m, where the influence of the surface waves no longer overpowers the record.

2.1.1 Determination of the optimal gauge length

The chosen G_L (10.2 m) is a compromise between high resolution, good SNR (Dean et al., 2016), and linearity (Hartog, 2017) in most of the envisaged GeoLab data applications, but it should be noted that varying angles of incidence and specific wavenumbers can change the response of a given G_L. For specific applications where better low-frequency response is desirable, longer G_Ls should be used (Hartog, 2017). Additionally, the sensitivity to strain along each G_L is not a linear function, and an impulse applied at the middle of the G_L will induce a larger phase shift than an impulse applied away from the middle of the G_L (Hubbard et al., 2022). In post-processing, longer G_Ls can be obtained by averaging neighbouring G_Ls, albeit at the expense of a decrease in spatial resolution.

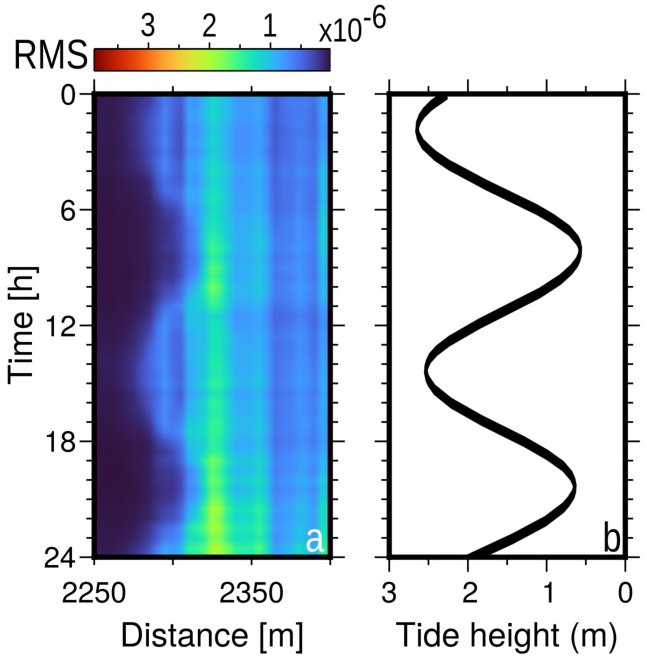

Figure 3 Tidal imprint on the phase rate observed at the section of the cable entering the sea. a) root mean squared (RMS) calculated on 5 min windows between 2.25 km to 2.45 km cable distance for the first 24 h of recording. b) Tide heights calculated for Funchal. Note that the tidal amplitude is less than 3 m, but the signal of the waves hitting the beach is discernible along a ~70 m slant distance.

Assuming a Ricker wavelet propagating axially, the 10.2 m G_L provides optimal SNR for signals between 60 Hz and 80 Hz travelling at the water sound velocity (Dean et al., 2016). For other sources of strain, the optimal G_L, $G_{L_{opt}}$, is determined by Eq. (6), where λ is the wavelength and r varies between 0.4 and 0.6 (Dean et al., 2016).

$$G_{L_{opt}} = r \cdot \lambda \quad . \tag{6}$$

Signal distortion occurs when r exceeds 1 (Dean et al., 2016; Cuny et al., 2024), which means that the present G_L ensures signal fidelity up to 150 Hz at 1500 m s^{-1}. Non-linear correlation between phase and strain also occurs when the signal is distributed over a G_L or more (Hartog, 2017).

2.2 Data quality

The data is generally very good, with most channels showing low noise (Fig. 2). Very localised, noisy channels indicate parts of the cable that may be going over rocks or narrow crevasses and are thus more exposed to

currents. The current-induced vibrations show a repetitive pattern with a period that indicates tidal modulation (Fig. 4). The noisier channels are at 9 km and 13 km cable distance.

To determine the location of noisy channels, a systematic calculation of RMS of the phase rate (Fig. 2) was performed for the entire dataset in 30 min windows. Outside the land and coastal domains where anthropic and ocean waves dominate the signal, a few limited cable sections are generally noisy. They are at ∼7 km, ∼9 km and ∼13 km, where the cable is believed to be suspended and exposed to currents, showing a quasi-tidal noise pattern (Fig. 4).

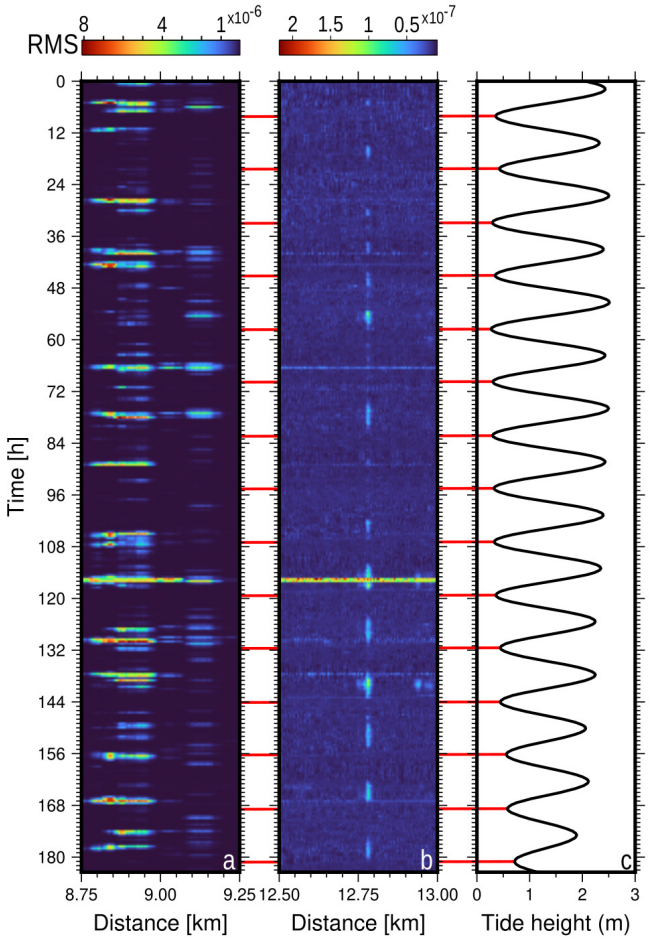

Figure 4 Tidal imprint on crosstalk events. a) RMS calculated on 5 min windows around ∼9 km cable distance. b) Same, for ∼12.75 km. Horizontal lines (e.g. at 116 h) are saturation events due to crosstalk(see Fig. 6). c) Tide heights calculated for Funchal. To aid in interpretation, horizontal red lines between a), b), and c) indicate low tides.

The average standard deviation of all channels during the acquisition period highlights the noisiest sections of the cable and shows a gradual increase in the noise levels as the distance increases (Fig. S4). The transition from the $1/f$ noise region to the broadband noise region (e.g., Cranch et al., 2003; Hartog, 2017; Vidal-Moreno et al., 2022) occurs at ∼10 Hz.

The noise spectral density (NSD) of a one-hour window for several subsets of channels was calculated (Fig. 5). A global NSD was calculated with a weighted sum of the individual channel subsets. The weights used were proportional to the number of channels in each subset. The global NSD is significantly influenced by channels near the coast, where noise primarily originates in Rayleigh waves propagating through the solid Earth (secondary microseisms), wind-driven ocean swells, or a combination of both. In the land domain, high-frequency anthropogenic noise is noticeable (Fig. 5, blue line). Beyond the coastal domain, noise from waves is still discernible (Fig. 5, green line). Daily spectrograms from 0.01 Hz to 125 Hz were calculated for 72 channels along the entire fibre (Figs. S5-S13), covering different domains and depths, to better characterise the frequency content of the signals and their variation during the acquisition period.

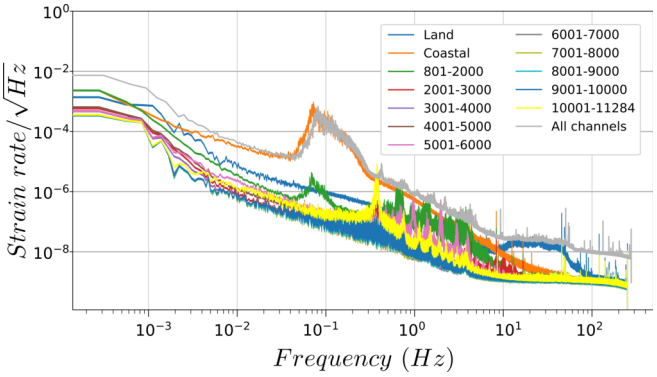

Figure 5 Noise spectral density. Different colours represent noise spectral density for various sections of the cable, calculated for a 1-hour window of strain rate data starting at 2023/10/27 15:20:00Z. *Land* and *coastal* indicate the groups of channels in the respective domains, as defined in Section 2.1 (see Fig. 2a). The noise spectral density for the entire cable was determined by calculating a weighted average of the noise spectral densities of its different parts.

Common-mode noise (Ajo-Franklin et al., 2019; Lindsey et al., 2020) arises from local disturbances near the interrogator, imprinting the same signal simultaneously across all channels. Such disturbances typically include strong vibrations from human activities or natural events, such as earthquakes. In this dataset, wideband common-mode noise was not observed. The interrogator was installed in a secure facility with no permanent staff, and the traffic on the roads around the landing station is light. The nearest recorded seismic event ($M > 2$) occurred on October 27th, approximately 70 km away, and did not generate sufficient ground motion to induce detectable common-mode noise in the recordings.

However, monochromatic pulses between 45 Hz and 50 Hz are present in all the spectrograms (see Fig. S5 and supplement), pointing to anthropic noise sources or crosstalk between the fibre and other utilities on the segment between the interrogator and the shore that is then imprinted on the rest of the data (e.g., magnetostriction noise from transformers or high voltage lines crossing the path of the cable, air conditioning fans or other equipment installed in the racks adjacent to the interrogator).

The dynamic range of DAS differs from that of traditional seismic sensors, as it saturates in different ways.

A critical step in deriving strain-induced changes in Rayleigh scattering-based DAS data is phase unwrapping, which commonly assumes phase continuity along the fibre. This requires the phase difference between consecutive measurements to remain below π, or cycle-skipping occurs. For single pulse DAS systems (Zhai et al., 2025), Eq. (4) can be rewritten for the theoretical maximum measurable strain rate before cycle-skipping occurs ($\dot{\varepsilon}_{saturation}$) as:

$$\dot{\varepsilon}_{saturation} = \frac{\lambda}{4\,n\,\xi}\frac{1}{G_L} \quad . \tag{7}$$

The OptoDAS interrogator, which uses sweep frequency pulses, is capable of unwrapping phase measurements up to $\pm 8\pi$, but the wrapping interval still scales proportionally with frequency and inverse proportionally with gauge length. These assumptions limit the dynamic range of DAS and may result in highly distorted record signals due to saturation (van den Ende et al., 2024) and cycle-skipping during strong ground-motion events, causing abrupt or very localised strain changes, excessive noise, or too low sampling rates (Cedilnik et al., 2019; Sun et al., 2024). While saturation in electronic sensors is a well-understood concept, the term is less accurate when applied to sweeping-frequency interrogators such as the OptoDAS used in this experiment. Here, what is often described as saturation is better understood as inter-channel crosstalk, arising mainly from the interaction between sweep length and phase unwrapping algorithms. When cycle-skipping occurs, the strain rate on the fibre exceeds the maximum rate the interrogator can resolve, resulting in data corruption that originates from beyond the crosstalk point. Stripe-like errors in waterfall plots are the usual indicator of crosstalk and cycle-skipping events (Sun et al., 2024). A crosstalk event indicates only an excessive strain rate for the given acquisition parameters rather than a fundamental inability of the system to measure large strain values. Shorter sweep lengths reduce the probability of crosstalk, but will limit the maximum sensing range.

Throughout the GeoLab dataset, several of these events are evident (see Figs. 2 and 6). Some are generated at the regions where the cable is believed to be suspended and exposed to currents, for example, the streak-like events that start at ∼9 km in Fig. 2 (∼116 h). Other events suggest more localised and sporadic sources. When crosstalk occurs, all the channels beyond that point are affected. On the immersed part of the cable, the identifiable events are primarily due to currents affecting the cable, as they repeatedly originate at the same cable offsets. On land, mechanical excitation of the cable, either at the landing station or due to heavy traffic over the cable conduit, may also cause crosstalk. On Fig. 2, these effects are clearly visible at 63 h, affecting the last 3 km, and at 116 h, from 9 km onwards. Additional saturation events are also identifiable on Fig. 4 (middle panel).

2.2.1 Coupling

Ground coupling affects the cable's response to the acoustic field. Accurately characterising this parameter is essential for combining different channels in algorithms that depend on known or consistent instrumental responses. Still, insufficient knowledge about site conditions in terms of spatial and temporal variability is usually a critical obstacle (Sladen et al., 2019).

The cable installation required trenching only in the shallowest waters. From there onwards, it was lowered into place by the cable-laying ship. To protect it from rocks on the island slope, the cable is armoured to an unknown extent. Since the time of installation, parts of the cable have sunken into the sediment to varying degrees, especially in the deep basin, where the sedimentary cover is thicker. It is probable, however, that some parts of the cable are resting over rocks and thus still exposed (see Section 2.2).

We calculated the cross-coherence between adjacent channel pairs to highlight potential ground coupling differences (Fig. S14). We found that only a few channels have a significantly different response from their immediate neighbours. The cause for the different responses can be attributed to multiple factors, ranging from local conditions to fibre twist (Bertholds and Dandliker, 1988; Lindsey et al., 2017). Higher frequencies are generally less coherent, except for the ∼50 Hz noise described in Section 2.2.

To characterise the sensitivity of the cable, we calculated the SNR by comparing the RMS values of background noise and seismic signals. Specifically, we used a 6 s window of background noise and a 6 s window centred around the theoretical arrival time of P waves from a M2.7 local seismic event (Fig. 7 and Section 2.3, Tab. S2). RMS values were derived from unfiltered data across all individual channels, except for some channels in the transition from the second to the third domains, where the energy of the swell overpowers all other signals (blue rectangle in Fig. S15). Swell waves, generated mainly by strong steady wind far offshore, have frequencies between 0.05 Hz to 0.2 Hz, which correspond to long wavelengths (100 m to 500 m). They propagate coherently along very long distances and, along with an irregular or faster change of the bathymetry of the seafloor, can affect the RMS values on DAS cable channels located deeper than the typical 500 m depth at which swell usually no longer affects the data (Lindsey et al., 2019).

For this event, ∼3000 channels have a SNR ratio above 3 dB, indicating good sensitivity (Zhu et al., 2019). ∼400 have SNR below 1 dB, indicating poor coupling and sensitivity. 8 channels were statistical outliers, consistently showing SNR ratios above 90 dB, when the greater majority of channels never goes above 60 dB, which may indicate saturation, most likely due to the cable being directly exposed to currents. The lower sensitivity indicated by this test does not account for factors such as cable geometry, mechanical coupling to the ground, type of arrival (P or S), or the azimuthal dependency of the fibre response. These results are consistent with what is observed in Fig. 7.

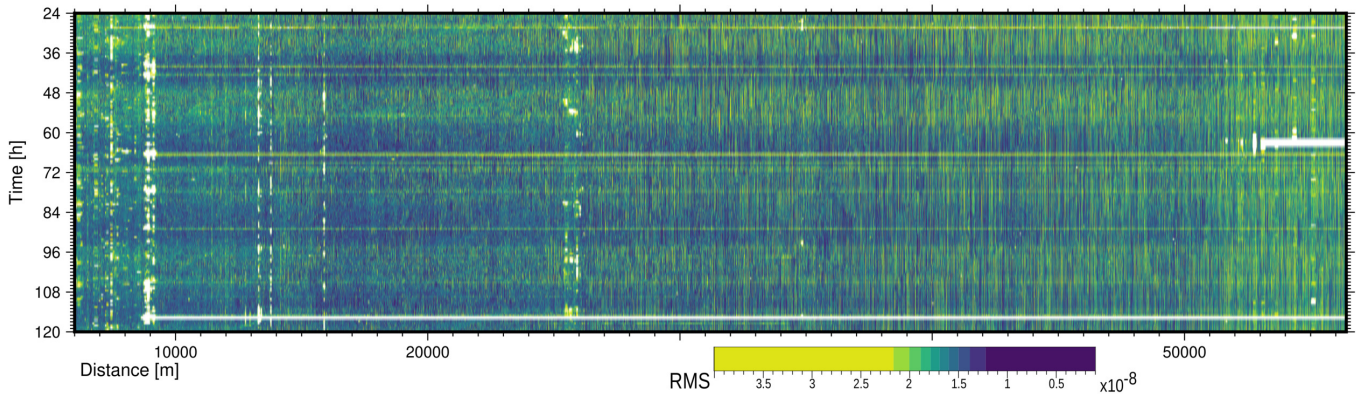

Figure 6 Saturation or crosstalk events. RMS calculated on 5 min windows. Horizontal streaks indicate parts of the record where a channel was saturated, i.e., a phase cycle-skip occurred. The first saturated channels correspond to cable sections presumed to be free-hanging. Tidal noise is also apparent.

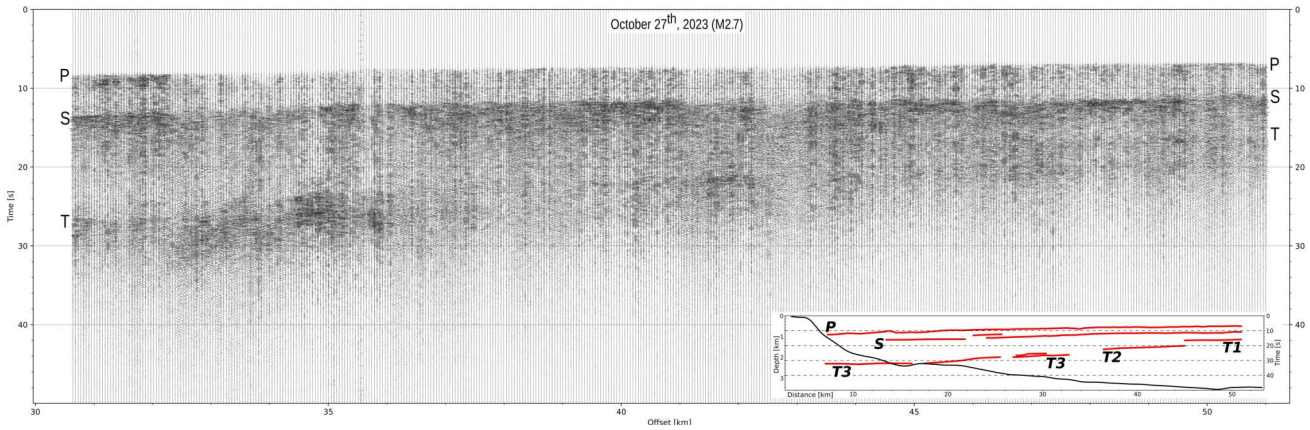

Figure 7 Record section. Excerpt of a record section for the 2023/10/27 M 2.7 event. 125 m trace spacing. Band-passed between 0.5 Hz and 20 Hz. Inset shows interpretation of P, S, and T arrivals, juxtaposed on the depth profile of the cable.

2.2.2 Ringing effects and spectral banding

Near the end of the fibre, prolonged ringing effects were detected after the arrival of the P and S waves from a local earthquake (Fig. 8). The ringing events slowly decay to background noise levels after more than 30 s. Each ringing event has a vertical axis of symmetry, with alternating polarities and varying in length from ∼90 m to ∼150 m. The spacing between each event is also variable, and increases towards the end of the fibre.

The earthquake appears to be the trigger, but the mechanism by which it was generated remains unknown.

On some days, groups of high-frequency regular oscillations (Fig. 9) are identifiable on spectrograms, modulated by a signal with a 10 min to 15 min period, and another with a 12 h to 15 h period.

These events may be linked to the ringing artefacts present after earthquakes, but their origin is, so far, unknown. Site effects appear to play an important role, as neighbouring channels show different banding patterns. This observation also seems to exclude common noise introduced at the start of the cable.

2.3 Seismicity

During the data acquisition period, two M>2 earthquakes within 250 km of Madeira Island (Tab. S2) were recorded by the Instituto Português do Mar e da Atmosfera (IPMA) network. Both events are recorded along the entire GeoLab fibre. Several other M>2 events were also detected in the Canary Islands region by the European-Mediterranean Seismological Centre (EMSC) network (see Tab. S2). These are generally only detected in the deeper parts of the cable, as their signal is overpowered by sea waves closer to the slope of Madeira Island. Teleseismic events were also recorded (see Tab. S2 and Fig. 10), including P waves, which, given their perpendicular incidence, are harder to record with DAS.

Five permanent broadband seismic land stations are located in the Madeira and Porto Santo Islands (Fig. 1). However, during the DAS acquisition period, only the stations PMPST and FUL were operational. The FUL station is equipped with a short-period seismometer (SH*), while the PMPST station has both a broadband seismometer (HH*) and an accelerometer (HN*). Especially in the deeper basin, events recorded by the fibre are easier to identify than on the land stations, mostly due to the number of channels available and lower noise levels.

On October 27,th 2023, a small earthquake (M 2.7) east

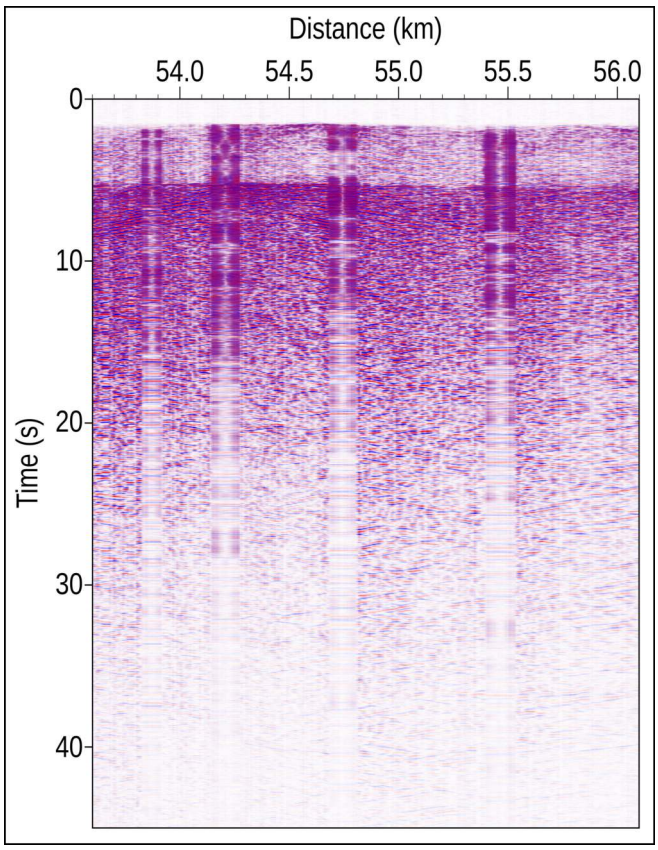

Figure 8 Ringing events. Unfiltered 250 Hz record section (501 channels) of a local M 2.7 event (see Section 2.3), from ∼53.6 km to ∼56.1 km cable distance. From right to left, the spacing between the narrow vertical bands decreases. Apart from the P arrival that triggers the ringing effect, no other earthquake signal is visible within these bands.

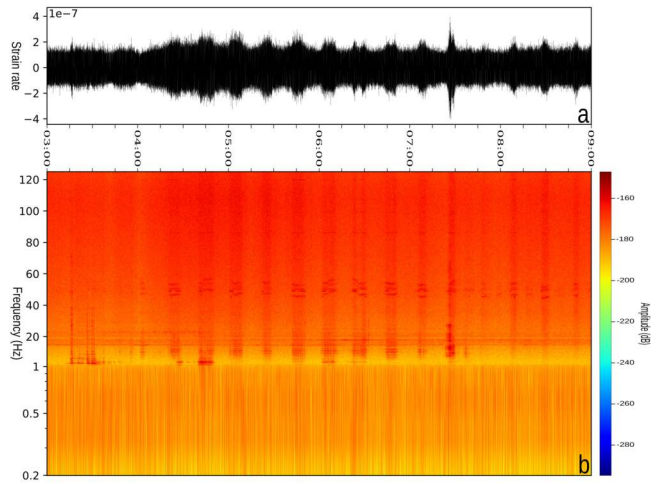

Figure 9 Modulated high-frequency spectral banding recorded on 2023/11/01, on a channel at ∼41.9 km cable distance. a) Phase rate. b) Spectrogram between 0.2 Hz and 125 Hz. $NFFT = 256$, overlap 50 %.

of the Desertas Islands (Fig. 1) was detected by land stations in Madeira, Porto Santo, Canary Islands, and also along the entire GeoLab fibre (Fig. 7). In addition to body waves (P and S), tertiary waves (T) were also recorded on the DAS cable. They were presumably generated at the bathymetric rise of the Desertas Islands, halfway between the epicentre and the GeoLab fibre, and recorded on the DAS cable. The three identifiable branches point to different points of conversion. The T phases are not identifiable on the land stations in either Madeira or Porto Santo. This is currently the nearest source recording of T phases using DAS or conventional instruments.

2.3.1 Broadband response

As local coupling conditions, the intrinsic directional sensitivity of DAS, and temperature and pressure contributions for the measured strain are factors that limit the long period response of DAS, the broadband sensitivity of DAS for seismic energy is a topic under active research (Becker et al., 2017; Ajo-Franklin et al., 2019).

On the record section, the arrivals of all major phases are easily identifiable, and directly comparable to those recorded on PMPST, a broadband seismic station in Porto Santo Island (Figs. 1 and 10b), c) and d)). On the stacked subsets, lacking the lateral continuity provided by multiple traces, identifying arrivals is more challenging but not impossible. Long-wavelength oscillations are visible on the unfiltered stacked channels.

We also extracted and stacked 6200 s of phase rate data on 100 channels between ∼28.1 km and ∼33.1 km (spacing ∼50 m), starting 2600 s before the predicted arrival of the P wave for the M_w 6.7 event near the coast of Chile that occurred at 2023/10/31 12:33:44Z. We applied several bandpass filters to the stacked channels to highlight different periods (Fig. S1).

2.4 Oceanographic parameters

Apart from deformation, DAS is also sensitive to pressure and temperature (see Section 1.2), but these quasi-static observations are inherently more challenging to analyse than impulsive events. One method to enhance their visibility involves computing mean phase rates over sufficiently large time windows (e.g., Ide et al., 2021). By using mean values instead of a low-pass filter, we treat each time window independently, creating snapshots. In this study, we introduce a normalisation step to balance the varying channel sensitivities and improve signal clarity: for each channel, the average phase rate μ, calculated over 30-minute windows, is divided by the overall standard deviation σ across all channels. This results in an effective estimate of the SNR:

$$\mathrm{SNR} = \frac{\mu}{\sigma} \quad . \tag{8}$$

In a final step, aimed at balancing noisy and calm periods, the median value of all channels is subtracted to each channel for each window. This analysis highlights slow-moving features (Fig. 11, for example, between 10 km and 25 km) with obvious tidal control, due to their semi-diurnal period (Fig. S2). These migration events occur repeatedly across the same channels and are more pronounced on the island's slope. Although DAS measures strain rate, the observed deformation on the slow-moving migration events in the deep basin is most likely not related to the actual deformation of the

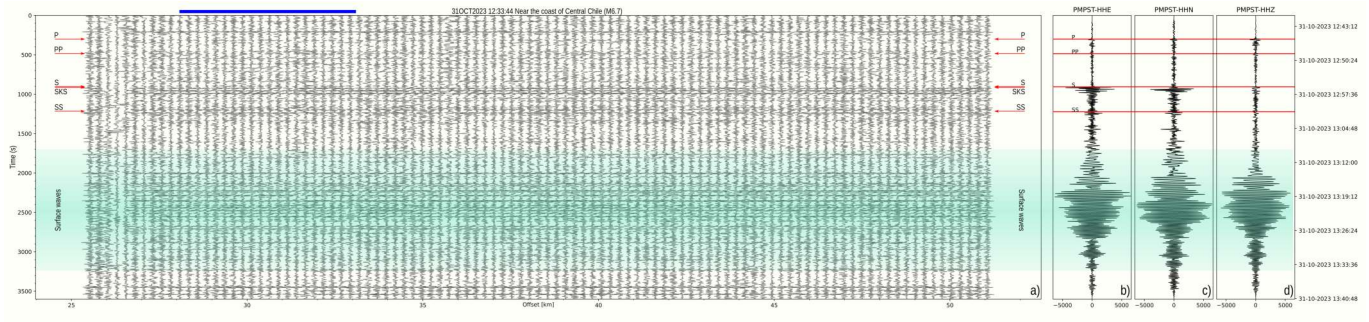

Figure 10 Record section of a teleseismic event. a) Excerpt of a 1 h record section for the M6.7 event that occurred near the coast of Central Chile on 2023/10/31 12:33:44Z, at a depth of 41 km and distance of 80.25° (8950 km). Showing one trace at every 255 m from ∼25.5 km to ∼51.1 km cable distance. Bandpass-filtered between 10 s and 100 s. Red arrows indicate predicted arrivals using TauP (Crotwell et al., 1999) with the iasp91 model (Kennett and Engdahl, 1991) for the coordinates of the first and last channel shown in the record section. Waveforms for the b) E, c) N and d) Z components of station PMPST, bandpass-filtered between 10 s and 100 s (Fig. 1). Red lines indicate the predicted arrivals for the station coordinates. The green band indicates surface wave arrivals. Coloured trace on top of the record section indicates the sections used for the broadband test on Fig. S1.

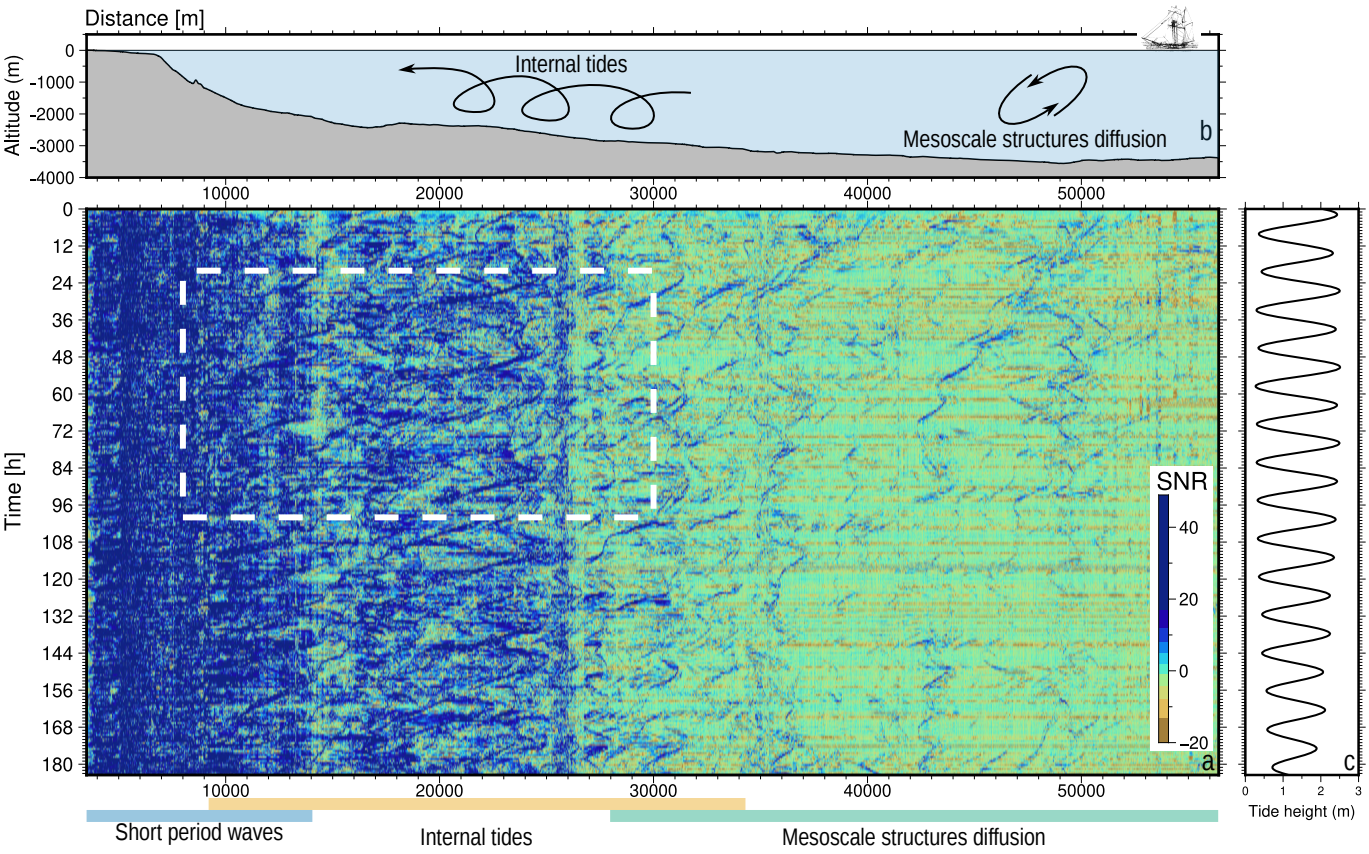

Figure 11 Global SNR map. a) Median-corrected signal-to-noise ratio for the entire dataset, calculated as the mean (μ) divided by the standard deviation (σ) in 30-minute windows for each individual G_L. At each time window, the median value of all channels is subtracted to each channel. The extension of the different domains is marked with coloured bands below the panel. Dashed rectangle indicates the region analyzed in Fig. S2. b) Depth profile along the cable track. Bathymetry source: GEBCO Compilation Group (2023). c) Tide heights modelled for Funchal.

fibre, but rather to changes in the refractive index and Rayleigh scattering of the fibre-optic cable due to water temperature variations (Dong, 2013; Ide et al., 2021; Williams et al., 2023). Relative temperature changes can be inferred from the apparent strain, but without external calibration, no absolute temperature values can be derived (Sinnett et al., 2020; Ide et al., 2021). The inferred temperature variations (Fig. 11) become weaker with increasing depth. Tidal influence seems to dominate at depths less than 1800 m, with stronger signals on the island slope. In the deep basin, the semi-diurnal pattern loses symmetry, which may indicate that the temperature fluctuations are linked to mesoscale events associated with the meandering of the Azores current (Käse and Siedler, 1982; Siedler et al., 2005; Frazão et al., 2021). At depths greater than 1800 m, internal waves

and other more complex oceanographic phenomena dominate. Tides and internal waves have also been studied in the Canary Islands, where a DAS dataset was recorded on a comparable bathymetric profile to the GeoLab fibre (Williams et al., 2023; Peláez Quiñones et al., 2023; González-Herráez, 2024).

2.5 Ocean waves and currents

The half-hour median power spectral density (PSD) along the first 1700 channels (∼8.7 km) clearly shows distinctions between the three different domains on land, in water on the narrow shelf, and in deeper water (Fig. 12). On the narrow shelf, a prominent peak can be observed in the first few kilometres in the ocean at 14 s, which vanishes at distances where the water depth reaches ∼100 m, consistent with Williams et al. (2022). In contrast to that study, a secondary peak at 7 s appears to be much weaker in our case and can only be detected against the background noise at a few channels very close to the coast (Fig. S16). These peaks, although seeming to show a double-frequency connection, are unlikely to be related due to the dispersion relation for free ocean surface gravity waves that the 6 s to 8 s follows:

$$\omega^2 = gk\tanh(kh) \quad . \tag{9}$$

Or, in the event of currents, the equation can be adapted to:

$$(\omega - Uk)^2 = gk\tanh(kh) \quad . \tag{10}$$

In both equations, ω is the angular frequency, g is the gravitational acceleration, k is the angular wave number, and h is the water depth. In addition, U is the apparent velocity of the current along the cable (Williams et al., 2019). It is possible to calculate the frequency at which the signal of ocean surface gravity waves falls below the instrumental noise floor, also known as f_c (Crawford et al., 1991; Williams et al., 2022):

$$f_c = \sqrt{\frac{g}{2\pi h n}} \quad . \tag{11}$$

This calculation depends on the maximum frequency at which these waves still affect the ocean bottom. In addition to mainly using the same variables as defined above, the variable $n = 2\pi/kh$ establishes the relation between wavelength and water depth and is in the range of 0.5 to 2.

The half-hour f-k spectrograms of the cable section on the narrow shelf exhibit a strong dominance of landward waves. Using a directional f-k filter, the landward and seaward waves can be separated (Fig. 13). This pattern is stable over the entire week of recording. Due to variations in the direction of swell and currents on small spatial and temporal scales, the results represent a combination of those effects, which do not entirely match the theoretical dispersion curves with or without an added parameter of current.

2.5.1 Estimation of speeds of deep currents

The present dataset can also be used to estimate current speed (but not velocity) from the analysis of the vibrations of suspended sections of the cable, providing essential insights into ocean bottom circulation at depths not easily instrumented (Flores et al., 2023; Spingys et al., 2024).

When a fluid flows past a non-streamline object, an unstable wake forms and alternating low-pressure vortices are shed downstream, causing alternating lift (side-to-side) and drag (front-to-back) forces to be applied to the object (Skop and Griffin, 1975; Griffin, 1985).

The frequency of vortex shedding is often characterised by the Strouhal number St, a dimensionless number that relates the frequency of vortex shedding f_{vort} to the fluid flow speed v and a characteristic length of the body L (usually its diameter) (Triantafyllou et al., 2016). The vortex shedding frequency is given by:

$$f_{vort} = St\frac{v}{L} \quad . \tag{12}$$

As the vortices cause vibrations in the objects, these vibrations, in turn, affect the formation of the vortices, establishing a feedback loop that can result in either stable or unstable dynamic equilibria (Triantafyllou et al., 2016). Stable equilibrium, or resonance, starts when the Strouhal frequency is close to the object's eigenfrequency (Feng, 1968) and, due to constructive interference, frequency gliding events occur until the lock-in regime is attained (Skop and Griffin, 1975; Griffin, 1985). This regime is characterised by a fundamental frequency and many sharply defined overtones, with turtle-shaped frequency gliding events (Essing et al., 2021) on the spectrograms (see Fig. 14). The amplitude of the oscillations (and strain) increases with current speed (Kovachev et al., 1997). Additionally, a suspended section of the cable can behave like a plucked string, generating persistent signals with stationary frequencies (Flores et al., 2023). These are distinguishable from the lock-in regime due to the absence of large amplitude events and well-defined harmonics.

The sections where the cable is suspended are generally noisier (see Figs. 2 and 4) than in the deep basin, due to the limited dynamic range of DAS. We used this characteristic as a way to quickly scrub the data, by assuming that in the lock-in regime, the oscillations of the suspended fibre sections induce sufficient strain to cause cycle skipping and crosstalk. The crosstalk events propagate along the entire fibre (see Section 2.2).

A spectrogram of the phase rate ∼6 km away from the presumed suspended section (at ∼9 km) shows time-dependent features with frequency gliding and high-amplitude harmonic oscillations when in the frequency lock-in regime (Fig. 14). The lock-in regime occurs at frequencies between ∼1.5 Hz and ∼2 Hz (see lowest frequencies on the multiple overtones events indicated by red arrows on Fig. 15). The fibre-optic cable has a diameter of 25 mm. Using Eq. (12), and assuming $St = 0.21$, a standard value for ocean bottom circulation (Stähler et al., 2018; Essing et al., 2021; Corela et al., 2023), we can estimate that the water is flowing around the cable at a minimum speed of ∼12 cm s^{-1} to ∼20 cm s^{-1}. Monitoring the oscillations of the cable in these suspended sections is also essential to determine if the cable is moving or risks being damaged by excessive strain.

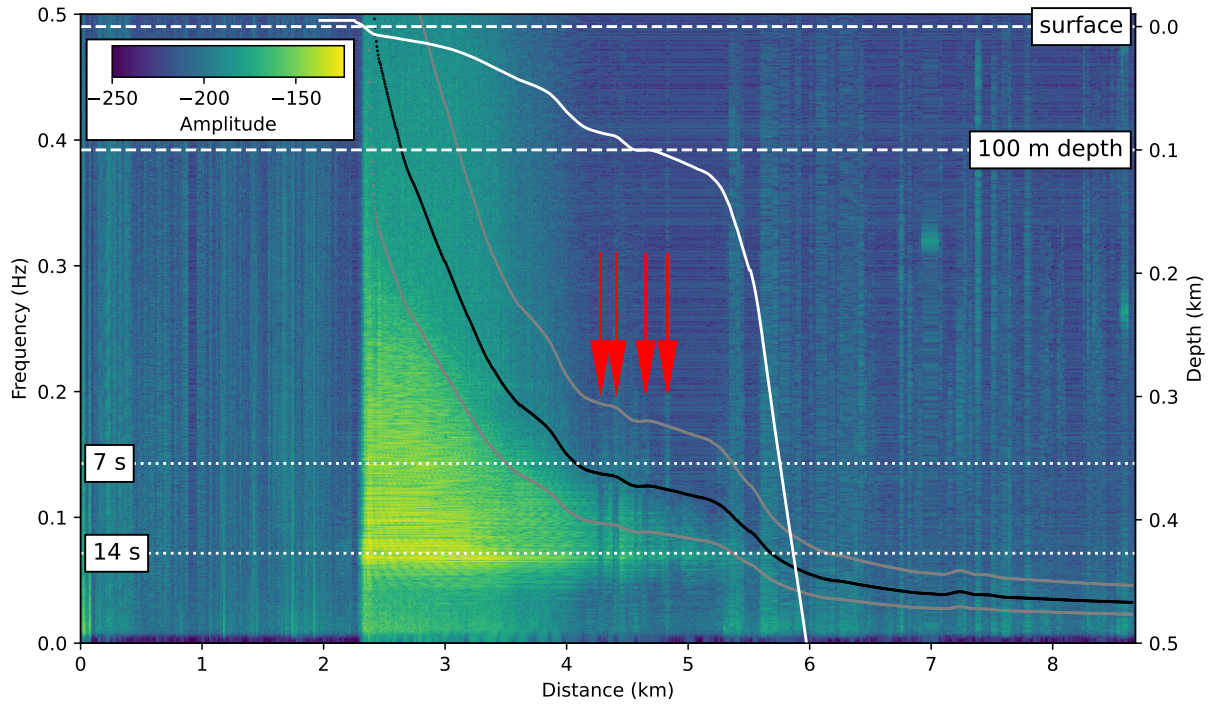

Figure 12 Median power spectral density of every channel in the first 1700 channels for a DAS recording over a 30-minute interval (start time: 2023/10/27 13:59:59Z), downsampled to 1 Hz and high-pass filtered with a corner frequency of 0.01 Hz. Cable depth is shown in white, the calculated f_c (Eq. (11)) are shown with a black line for a wavelength to water depth ratio of 1 (Williams et al., 2022) and with grey lines for limits of 0.5 and 2 (Crawford et al., 1991). Red arrows point to sections with low SNR.

2.6 Baleen whale vocalisations

Whale calls have previously been studied with DAS (Bouffaut et al., 2022; Landrø et al., 2022; Wilcock et al., 2023; Xiao et al., 2025). At a 500 Hz sampling rate, the dataset can faithfully record lower-frequency vocalisations of baleen whales of the North Atlantic Ocean up to ∼200 Hz—full vocalisations of blue, fin, sei and Bryde's whales, as well as low-frequency components of minke and humpback whales (or aliased parts of their low-frequency vocalisations). The acoustic repertoire of fin and blue whales, with a maximum frequency of ∼140 Hz (e.g., Watkins, 1981; Delarue et al., 2009; Pereira et al., 2020a; Miller et al., 2021), will be fully recorded. Bryde's whale calls, mostly studied in the Pacific Ocean (Rice et al., 2014), also exhibit low-frequency characteristics that can be potentially recorded, but the acoustic behaviour of the species in the North Atlantic is less understood. Sei whales are more commonly sighted in the Azores than in Madeira, although there are individuals that migrate between the two archipelagos (Prieto et al., 2014). The vocal repertoire of sei whales exhibits a wide range of frequencies, including low-frequency tonal downsweeps (<100 Hz) (Baumgartner et al., 2008), as well as mid- to high-frequency vocalisations (1 kHz to 5 kHz), that fall outside the recording capabilities of the current dataset (Cerchio and Weir, 2022). Humpback whales around the Macaronesia region are known to migrate to their breeding grounds in Cape Verde during winter and spring. Still, in Madeira, they are considered a rare species (Wenzel et al., 2020). Studies show a different seasonal pattern in the area for minke whales, suggesting a peak in occurrence during summer (Valente et al., 2019).

Fin whales are more abundant in the region from Autumn to Spring, with some populations remaining in the same area throughout the year instead of migrating (Notarbartolo-di Sciara et al., 2003; Delarue et al., 2009; Silva et al., 2013). In acoustic datasets, their calls are typically one order of magnitude more numerous than those of other whales (Romagosa et al., 2020).

Male fin whales produce downsweep signals between ∼30 Hz and ∼15 Hz, with an average duration of 1 s, called the 20 Hz call; backbeats at a constant frequency between 18 Hz and 20 Hz, lasting ∼0.8 s; and a 40 Hz sweep signal from 75 Hz to 40 Hz, called the 40 Hz call (Hatch and Clark, 2004; Romagosa et al., 2020). In some regions of the North Atlantic, they also produce upsweeps at 118 Hz and 140 Hz (Hatch and Clark, 2004). All of these signals are primarily produced in groups with a stereotyped interval, that can last for hours, with interruptions ranging from 1 min to 1 h (Watkins et al., 1987).

North Atlantic blue whales produce long, patterned, repeated sequences of low-frequency signals between 15 Hz and 20 Hz, which can be organised into phrases (Mellinger and Clark, 2003). These signals include a constant frequency tonal sound at ∼18 Hz, lasting ∼8 s, designated by Unit A, which is generally accompa-

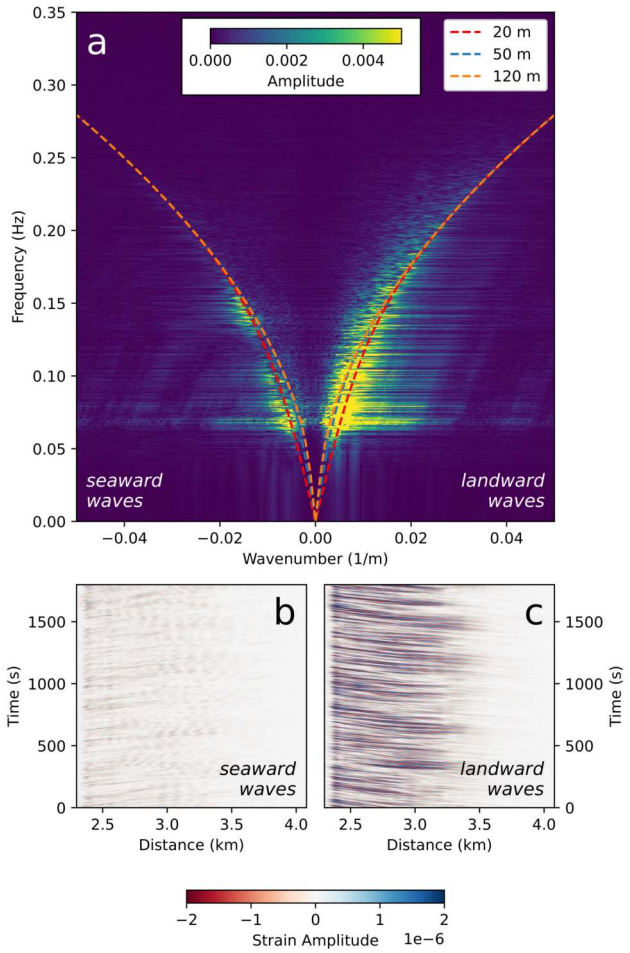

Figure 13 Dispersion curves for the section of the cable subject to ocean waves. DAS recording over a 30-minute interval in the water close to the beach (start time: 2023/10/27 13:59:59Z; channels 450 to 800: ∼2.30 km to ∼4.09 km), bandpass filtered between 0.04 Hz and 0.35 Hz. a) Frequency-wavenumber spectrum. Theoretical dispersion curves without added currents are shown for water depths of 20 m, 50 m and 120 m, which covers the extent of the cable on those channels, based on Eq. (9). Negative wavenumbers show the seaward direction of waves, and positive wavenumbers show the landward direction. b) Data after applying a directional f-k filter of 5 km s^{-1} to 50 km s^{-1}, limiting the output to seaward waves. c) Data after applying the same f-k filter, but limiting the output to landward waves.

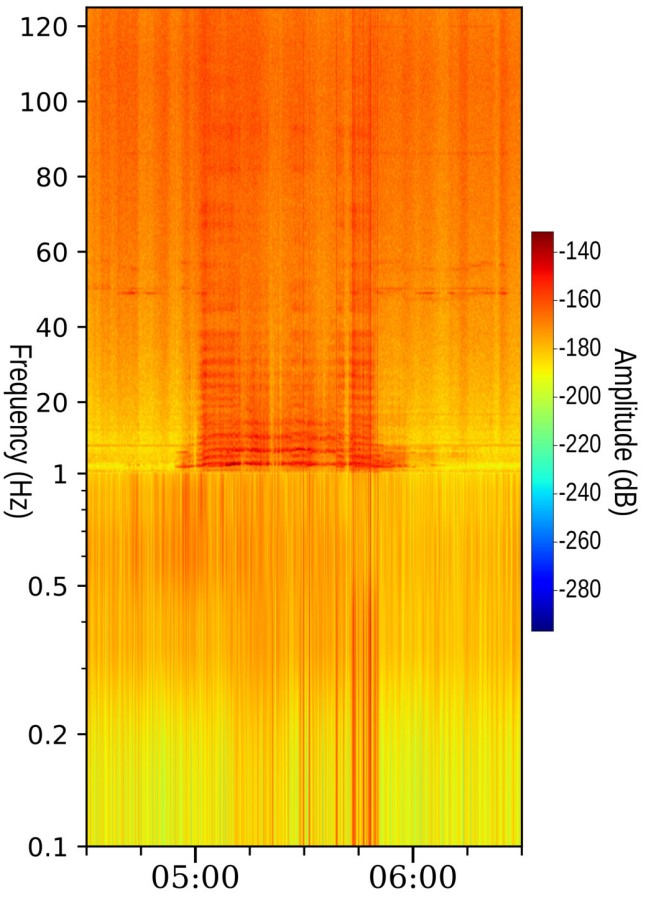

Figure 14 Lock-in regime. Spectrogram for channel at ∼11.2 km cable distance, between 0.1 Hz to 125 Hz on October 31th, highlighting the numerous overtones and turtle-shaped frequency gliding event. $NFFT = 256$, overlap 50 %.

nied by unit B, a ∼11 s-long downsweep from 19 Hz to 15 Hz (Cummings and Thompson, 1971; McDonald et al., 2006). Less commonly, sequences of only A or B parts are also found. Blue whales produce two additional tones, the 9 Hz sound, lasting from 2 s to 5 s that until now has only been observed with the A and B units, and the *arch sound*, a 5 s to 7 s sweep inflexion up to ∼70 Hz and then down to 25 Hz (Mellinger and Clark, 2003). The *arch sound* is not considered a song call, but rather linked to feeding behaviours and is produced by both sexes (Miller et al., 2024)

The low frequency calls of sei whales are characterised by a ∼1.0 s to ∼1.4 s downsweep from 100 Hz to ∼20 Hz or from 100 Hz to ∼40 Hz. However, there is still debate whether these are variations of the same call or if different populations share the same acoustic signals (Baumgartner et al., 2008; Johnson et al., 2014; Romagosa et al., 2015; Nieukirk et al., 2020). Some characteristics of sei whale downsweeps can be very similar to the downsweeps produced by other baleen whales. Still, sequences of these sounds can be identified by their shorter interval between calls.

The humpback whale signals that this dataset is capable of recording entirely are *wops* and *thwops*, brief harmonic upsweeps at fundamental frequencies below 60 Hz (Dunlop et al., 2007, 2008; Stimpert et al., 2011). Other higher-frequency signals will be partially or completely aliased.

Using hydrophones and in favourable conditions (low background noise and sensors in the sound fixing and ranging (SOFAR) channel), whale vocalisations can be detected up to hundreds of kilometres (Payne and Webb, 1971; Širović et al., 2007; Helble et al., 2020; Pereira et al., 2020a), and multi-path arrivals that bounce several times between the ocean floor and surface are also routinely recorded (Širović et al., 2007; Matias and Harris, 2015; Hilmo and Wilcock, 2024). With DAS, the detection range is usually in the tens of kilometres (Bouffaut et al., 2022; Wilcock et al., 2023), although the parts of the cable within the SOFAR channel

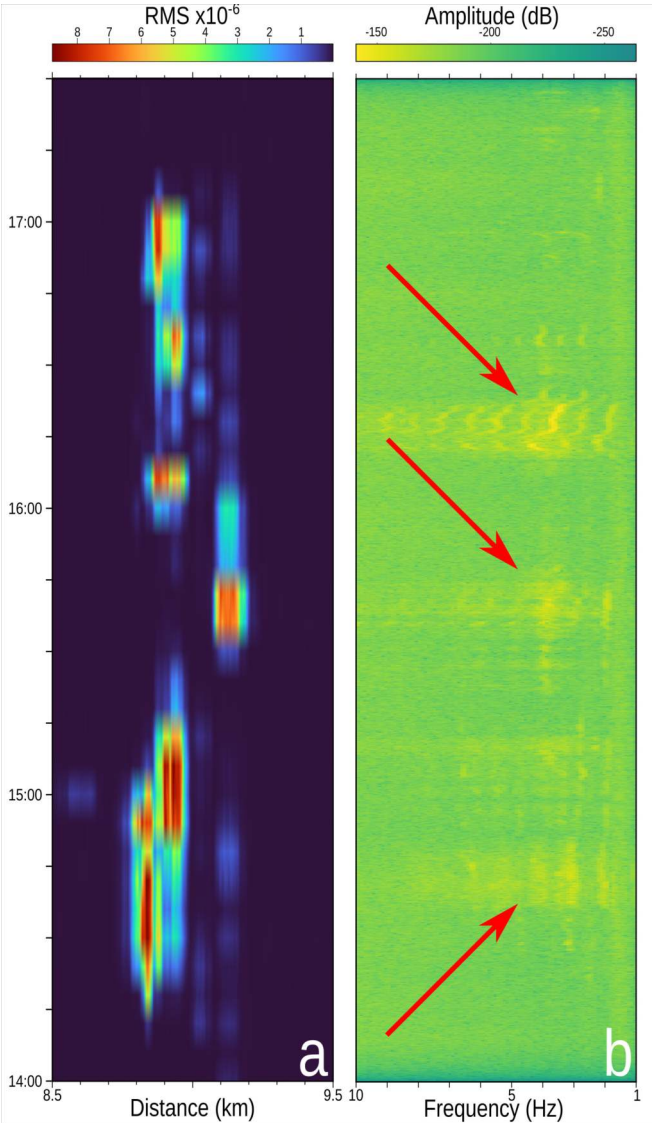

Figure 15 High-amplitude cable oscillations. a) RMS calculated on 5 min windows between 8.5 km to 9.5 km cable distance, from 14:00:00 to 17:30:00 of October 26th. b) Spectrogram for channel at ∼15.3 km cable distance, between 1 Hz to 10 Hz, highlighting vortex shedding events with frequency lock-in and gliding. $NFFT = 256$, overlap 50 %. Red arrows point to high-amplitude harmonic overtones.

are expected to show greater sensitivity. When compared to hydrophones, the SNR of DAS is significantly lower (Douglass et al., 2023), also because the cable is on the seafloor. Poor broadside sensitivity is commonly cited as a limiting factor (Lindsey et al., 2020), but acoustic waves can be detected in all directions except broadside.

Daily spectrograms from 1 Hz to 50 Hz on channels in the deep basin and on the island slope were manually scrubbed to identify characteristic vocalisation patterns of whales. Shorter time windows were then used to classify the identified calls.

Signals from at least two baleen whale species have been confirmed in the recordings: the 20 Hz fin whale call and the sei whale downsweep. The recordings of the fin whale call displayed the typical stereotyped sequence, with intervals between calls (ICI) of ∼13 s seconds. Sei whale downsweeps appear in the recordings as doublets and in quick sequences of 5 to 8 calls (Fig. 16c), with a short ICI of ∼4 s.

2.7 Other biological sounds

Additional events of possible biological origin are found throughout the dataset, especially at intermediate depths, where the sedimentary cover is less thick. On the island slope domain, on October 29th, strong signals are detectable on the dataset for several hours, between ∼10 km and ∼25 km cable distance, including multi-path signals reflected from the sea surface and seafloor (blue arrows on Fig. 16a). Multi-path arrivals can be used to estimate depths and ranges (Pereira et al., 2020b). From the shape of the hyperbola on Fig. 16a, assuming an average sound propagation velocity of 1.5 km s^{-1}, and making no corrections for depth, we estimate that the signals are recorded up to ∼6 km slant range. We currently classify these signal as baleen whale signal of either fin or, less likely, blue whale. The unclear identification stems from the signal not fitting any of the canonical calls for either fin or blue whales. Two common 20 Hz fin-whale note types have been described: an A-type with higher centre frequencies (∼18 Hz to 28 Hz) and a B-type with lower frequencies (∼13 Hz to 23 Hz). The backbeat, a distinct fin-whale component near ∼18 Hz, is sometimes mislabelled as a B-type call. The 15 Hz to 22 Hz energy in Fig. S18 is consistent with the bandwidth of a B-type call. However, the downsweep slope and the ∼53 s interval between signals are atypical for fin whale notes. Low-frequency downsweeps with inter-call intervals greater than 50 s have at times been attributed to blue whale D calls (for e.g. Wiggins et al., 2005; Oleson et al., 2007; Lewis and Širović, 2018). D-calls are notably variable in frequency extent and timing and often begin above 25 Hz to 30 Hz (Miller et al., 2022). The sweeps in Fig. S18 do not clearly match canonical D-call contours, but their intervals are more consistent with blue-whale signals. An alternative is that this signal are sparse fin whale 20 Hz notes occurring at unusually long inter-note intervals.

Other possible biological signals were also found in the deep basin (Fig. 16d). In the frequency domain, they share some shape-wise similarities with humpback whale *wop* and *thwop* signals, but their duration exceeds any known example of humpback calls. They are currently classified as of unknown biological origin.

2.8 Ship noise

Unlike other regions where submarine DAS data has been studied (Rivet et al., 2021; Wilcock et al., 2023), the waters nearest to Madeira do not experience heavy traffic from bulk carriers. The major shipping lanes connecting Europe to North and South America run north and south of Madeira Island, well away from the fibre path. Funchal is a common destination for large cruise ships, but only a fraction of those making port calls in Funchal cross the Atlantic Ocean. Nonetheless, there are regular container and bulk cargo services between the Madeira and Azores ports, as well as smaller fishing

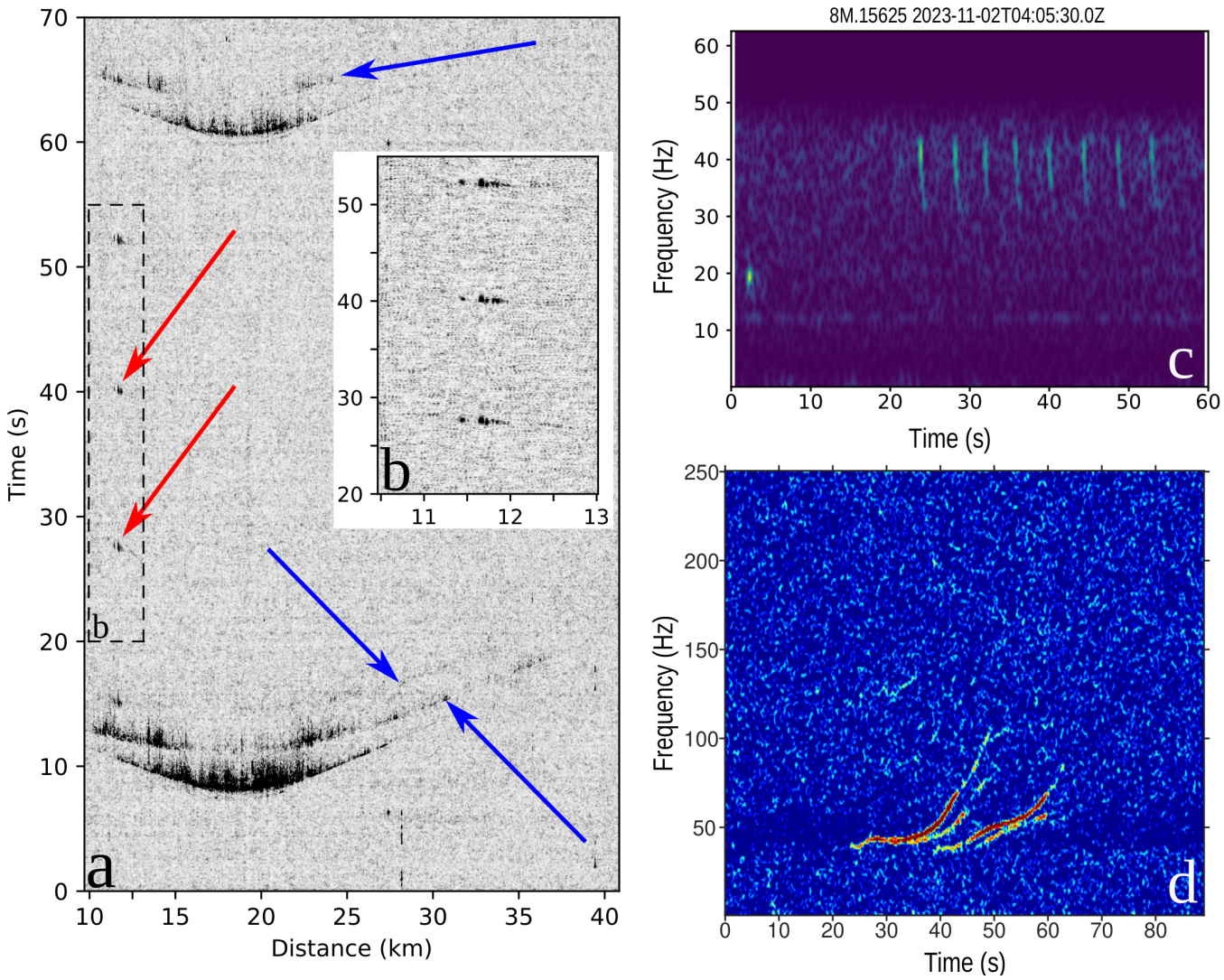

Figure 16 Baleen whale calls and other biological sounds. a) Time-distance plot of multiple whale calls. Data were filtered with an 8th order bandpass Butterworth filter between 12 Hz and 22 Hz, as well as an f-k filter to remove energy with an apparent velocity along the cable below 1.4 km/s. Data starts at 2023/10/29 04:52:29Z. At ∼11.7 km, the red arrows indicate fin whale 20 Hz calls with ∼13 s inter-note interval. Due to their distance, they are only detected on a small portion of the cable. b) A zoom of the region defined by the dashed line in a) (see also Fig. S17 for a spectrogram). Blue arrows indicate multi-path signals for the large hyperbolic events centred at ∼20 km, likely fin or blue whale calls (see also Fig. S18 for a spectrogram). c) Sei whale calls. 60 s spectrogram of data from a channel at ∼15.6 km cable distance (start time: 2023/11/02 04:05:30Z). The single event at ∼20 Hz is a probable fin whale backbeat, although no downswept call is visible. To highlight the signal, data was filtered with an 8th order lowpass 50 Hz Butterworth filter. $NFFT = 256$, overlap 50 %. d) Possible biological signal. Spectrogram of 90 s of data from a channel at ∼39.3 km cable distance starting at 2023/11/02 17:58:00Z, showing possible biological signals. Equalised by subtraction of the average noise levels. The time-distance plot for this signal is shown in Fig. 17, where the channel location and spectrogram window length are indicated by a red arrow and line, respectively. $NFFT = 512$, overlap 95 %.

and recreational vessels that might travel over the cable. Logs of ship movements from the Madeira and Azores ports indicate that only six large ships, including cruise ships, are likely to have crossed the cable path during the acquisition period. Departures, arrivals, and routes of fishing ships are not recorded as the origin and destination ports are the same. Through manual scrubbing, we identified several signals that can be attributed to ships (Fig. 17) due to their artificial signature. Although it could be expected that the signals at the apex of the hyperbolas would be weak, as the acoustic energy is arriving broadside to the fibre, the G_L used is several times smaller than the observed wavelengths. A similar effect was observed by Bouffaut et al. (2025), when comparing apex sensitivity for datasets acquired with G_Ls varying from 4 m to 51 m.

2.9 Land observations

In addition to marine observations, the on-land part between the start of the cable and the end of the beach, where the swell is observed, can be used to monitor vehicle traffic (e.g., Ugalde et al., 2021). In this case, the f-k spectrum does not show the characteristic dispersion curves of ocean waves. Instead, due to the ca-

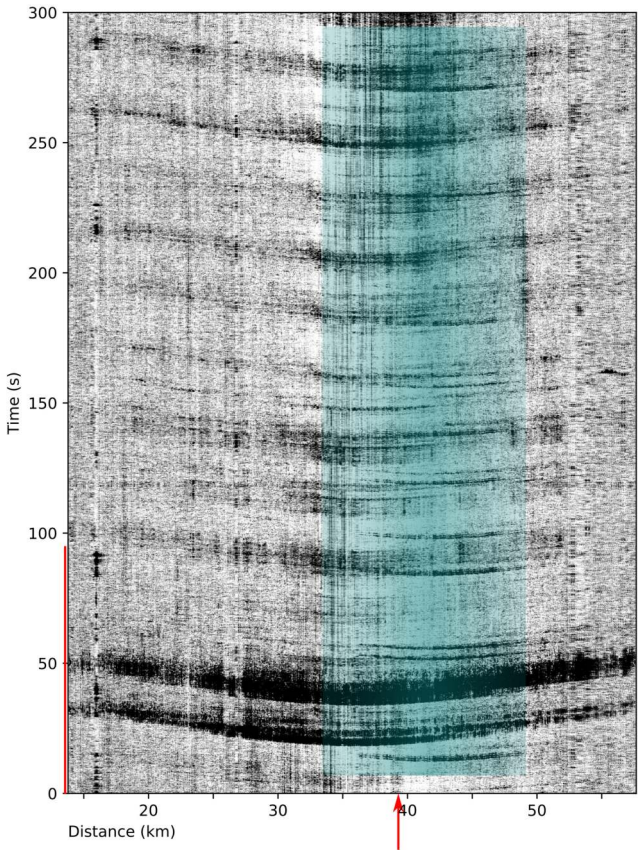

Figure 17 Ship noise. Time-distance plot (start time: 2023/11/02 17:58:00Z). Data was filtered with an 8th order bandpass Butterworth filter between 10 Hz and 40 Hz, as well as an f-k filter to remove energy with an apparent velocity along the cable below 1.4 km/s. Ship noise is highlighted with a green box. The broad swath centred at ∼50 s is the biological sound identified in Fig. 16d). Red arrow and line refer to channel location and window length of Fig. 16d).

ble location mostly sub-parallel to roads, vehicle traffic maps show close to linear patterns on the DAS recording (Fig. 18a) and the f-k spectrum (Fig. 18b), where it follows the relation

$$\omega = vk \quad , \tag{13}$$

with ω and k being angular frequency and wave number, and v the traffic velocity. Unlike marine observations close to the beach that show clear landward directional dominating features, the traffic can be traced in either direction. Individual sections may still be dominated by a single direction of movement, which can be caused by one-way streets, street gradients, or the side of the road on which the cable is located. The majority of vehicle speeds can be detected around 30 km h^{-1}, occasionally reaching up to 50 km h^{-1}, and rarely exceeding that.

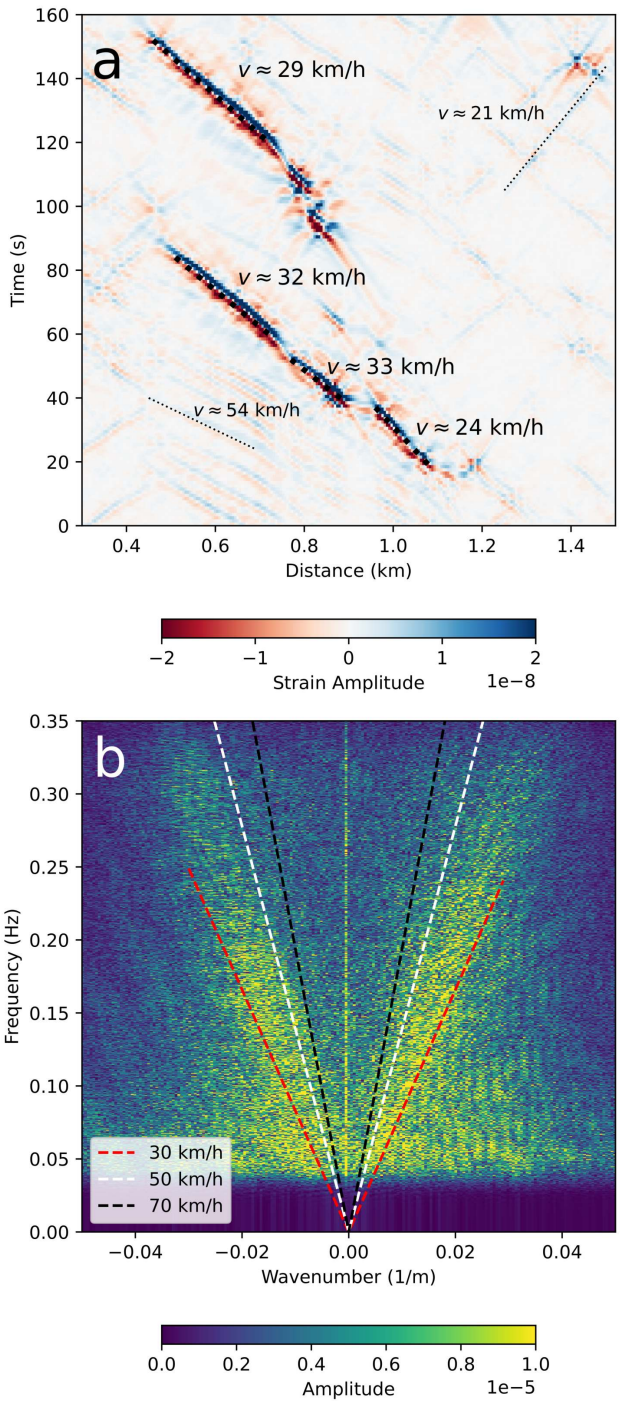

Figure 18 Vehicles moving. DAS recording on land (start time: 2023/10/27 13:59:59Z). a) Subsection of 160 s, showing individual vehicles, as well as calculated velocities of a selection. b) Frequency-wavenumber spectrum of a 30-minute recording (channels 50 to 430 ∼0.25 km to ∼2.20 km), bandpass filtered between 0.04 Hz and 0.35 Hz. Constant velocities are shown as coloured dashed lines.

3 Conclusions

The GeoLab dataset offers a unique opportunity to investigate the interactions between the ocean and the solid Earth, as well as the ocean's soundscape. The examples provided in this report highlight the many research opportunities made possible by DAS in offshore Madeira Island, including water column sound propagation, local seismicity characterisation, crustal imaging, and Early Warning systems. Future work on the GeoLab fibre will focus on obtaining empirical transfer functions for different parameters along selected seg-

ments of the fibre, utilising the deployment of broadband seismometers, hydrophones, and current meters in the vicinity of the cable. For marine mammal monitoring, the GeoLab dataset will fill a crucial gap in our knowledge of the various whale species present in Madeira, which have been studied in detail only in other parts of Macaronesia. Continued DAS observations will allow us to gain better insights into the seasonal distribution, migratory patterns, and the evolution of the vocal repertoire of whales around Madeira Island.

The objective of OOM is to continuously acquire DAS data, with a buffer of a few months before deleting full-resolution data. Continuous real-time data transmission to IPMA of 20 channels along the fibre will improve the azimuthal coverage of the Portuguese seismic observation network (Carrilho et al., 2021).

Acknowledgements

The authors express their gratitude to Carlos Lucas, coordinator of the Oceanic Observatory of Madeira, and Sandro Correia, from Empresa de Electricidade da Madeira, S.A., for their efforts and constant availability in setting up the interrogator at the GeoLab fibre. The authors also acknowledge EMACOM — Telecomunicações da Madeira, Unipessoal, Lda., for providing exceptional conditions for the installation of the equipment. OBSPy (Beyreuther et al., 2010) and Generic Mapping Tools (Wessel et al., 2019) were extensively used in the data processing and figure creation. The authors express their gratitude to Dr. Takashi Tonegawa and the two anonymous reviewers for their insightful and constructive comments, which significantly enhanced the manuscript. We also extend our thanks to the Editor, Dr. Wenbo Wu, for his valuable guidance and thoughtful feedback throughout the review process.

Data availability

The network code for GeoLab is *8M* (Loureiro, 2023) and the dataset used in this article is available through FDSN, with network code *3X* (Loureiro, 2024), in both full-resolution phase rate HDF5 files and decimated miniSEED files. Access to the dataset is restricted until January 2026 and will be openly available thereafter. HDF5 files are sampled at 500 Hz, with a gauge length of 1.2 m and spacing of 5.1 m, stored in ten-second blocks, from 2023/10/26 09:45:39Z to 2023/11/03 09:39:29Z, for a total volume of ∼7 TB. MiniSEED files are low-pass filtered, downsampled to 125 Hz, and spatially decimated to one channel per 102 m, totalling ∼380 GB. The present dataset will be permanently available.

A stationXML is available with the miniSEED files, describing the filtering stages, estimated dips and azimuths at each channel, and providing cable coordinates degraded to ∼200 m precision, which is consistent with those available from public documents and official cartography sources.

Competing interests

The authors have no competing interests, nor do they work for, advise, own shares in, or receive funds from any organisation that could benefit from this article. They have declared no affiliations apart from their research organisations.

Funding

This work is supported by the Portuguese Fundação para a Ciência e Tecnologia, FCT, I.P./MCTES through national funds (PIDDAC): UID/PRR/50019/2023, LA/P/0068/2020, and UID/PRR/50019/2025; and by the MODAS project 2022.02359.PTDC. The authors acknowledge support from the Geo-INQUIRE (GA 101058518) and SUBMERSE (GA 101095055) projects. Geo-INQUIRE is funded by the European Commission under project number 101058518 within the HORIZON-INFRA-2021-SERV-01 call. SUBMERSE is funded by the European Commission under grant agreement number 101095055 within the HORIZON-INFRA-2022-TECH-01 call.

References

Ajo-Franklin, J. B., Dou, S., Lindsey, N. J., Monga, I., Tracy, C., Robertson, M., Tribaldos, V. R., Ulrich, C., Freifeld, B., Daley, T., and Li, X. Distributed Acoustic Sensing Using Dark Fiber for Near-Surface Characterization and Broadband Seismic Event Detection. *Scientific Reports*, 9(1), February 2019. doi: 10.1038/s41598-018-36675-8.

Baumgartner, M. F., Van Parijs, S. M., Wenzel, F. W., Tremblay, C. J., Carter Esch, H., and Warde, A. M. Low frequency vocalizations attributed to sei whales (Balaenoptera borealis). *The Journal of the Acoustical Society of America*, 124(2):1339–1349, August 2008. doi: 10.1121/1.2945155.

Becerril, C., Sladen, A., Ampuero, J.-P., Vidal-Moreno, P. J., Gonzalez-Herraez, M., Kutschera, F., Gabriel, A.-A., and Bouchette, F. Towards tsunami early-warning with Distributed Acoustic Sensing: Expected seafloor strains induced by tsunamis [preprint]. *ESS Open Archive*, March 2024. doi: 10.22541/essoar.171052484.46251426/v1.

Becker, M. W., Ciervo, C., Cole, M., Coleman, T., and Mondanos, M. Fracture hydromechanical response measured by fiber optic distributed acoustic sensing at milliHertz frequencies. *Geophysical Research Letters*, 44(14):7295–7302, July 2017. doi: 10.1002/2017gl073931.

Benjumea, B., Gaite, B., Schimmel, M., Bohoyo, F., Spica, Z. J., Mancilla, F. D. L., Li, Y., Almendros, J., and Morales, J. Subsurface Imaging in Urban Areas With Ambient Noise Using DAS and Seismometer Data Sets: Granada, Spain. *Journal of Geophysical Research: Solid Earth*, 129(11), November 2024. doi: 10.1029/2024jb029820.

Bertholds, A. and Dandliker, R. Determination of the individual strain-optic coefficients in single-mode optical fibres. *Journal of Lightwave Technology*, 6(1):17–20, 1988. doi: 10.1109/50.3956.

Beyreuther, M., Barsch, R., Krischer, L., Megies, T., Behr, Y., and Wassermann, J. ObsPy: A Python Toolbox for Seismology. *Seismological Research Letters*, 81(3):530–533, 2010. doi: 10.1785/gssrl.81.3.530.

Blanc, W., Schenato, L., Molardi, C., Palmieri, L., Galtarossa, A., and Tosi, D. Distributed fiber optics strain sensors: from long to

short distance. *Comptes Rendus. Géoscience*, 354(S1):161–183, December 2022. doi: 10.5802/crgeos.129.

Bouffaut, L., Taweesintananon, K., Kriesell, H. J., Rørstadbotnen, R. A., Potter, J. R., Landrø, M., Johansen, S. E., Brenne, J. K., Haukanes, A., Schjelderup, O., and Storvik, F. Eavesdropping at the Speed of Light: Distributed Acoustic Sensing of Baleen Whales in the Arctic. *Frontiers in Marine Science*, 9, 2022. doi: 10.3389/fmars.2022.901348.

Bouffaut, L., Goestchel, Q., Rørstadbotnen, R. A., Sladen, A., Hartog, A., and Klinck, H. Estimating sound pressure levels from distributed acoustic sensing data using 20-Hz fin whale calls. *JASA Express Letters*, 5(4), April 2025. doi: 10.1121/10.0036351.

Bucaro, J. A., Dardy, H. D., and Carome, E. F. Fiber-optic hydrophone. *The Journal of the Acoustical Society of America*, 62 (5):1302–1304, November 1977. doi: 10.1121/1.381624.

Budiansky, B., Drucker, D. C., Kino, G. S., and Rice, J. R. Pressure sensitivity of a clad optical fiber. *Appl. Opt.*, 18(24):4085–4088, Dec 1979. doi: 10.1364/AO.18.004085.

Capdeville, Y. and Sladen, A. DAS sensitivity to heterogeneity scales much smaller than the minimum wavelength. *Seismica*, 3(1), 2024. doi: 10.26443/seismica.v3i1.1007.

Carrilho, F., Custódio, S., Bezzeghoud, M., Oliveira, C. S., Marreiros, C., Vales, D., Alves, P., Pena, A., Madureira, G., Escuer, M., Silveira, G., Corela, C., Matias, L., Silva, M., Veludo, I., Dias, N. A., Loureiro, A., Borges, J. F., Caldeira, B., Wachilala, P., and Fontiela, J. The Portuguese National Seismic Network—Products and Services. *Seismological Research Letters*, feb 2021. doi: 10.1785/0220200407.

Cedilnik, G., Lees, G., Schmidt, P. E., Herstrom, S., and Geisler, T. Pushing the Reach of Fiber Distributed Acoustic Sensing to 125 km Without the Use of Amplification. *IEEE Sensors Letters*, 3 (3):1–4, March 2019. doi: 10.1109/lsens.2019.2895249.

Celli, N. L., Bean, C. J., and O'Brien, G. Full-waveform simulation of DAS records, response, and cable-ground coupling. *Geophysical Journal International*, 2023. doi: 10.1093/gji/ggad449.

Cerchio, S. and Weir, C. R. Mid-frequency song and low-frequency calls of sei whales in the Falkland Islands. *Royal Society Open Science*, 9(11), November 2022. doi: 10.1098/rsos.220738.

Cole, J. H., Johnson, R. L., and Bhuta, P. G. Fiber-optic detection of sound. *The Journal of the Acoustical Society of America*, 62(5): 1136–1138, November 1977. doi: 10.1121/1.381647.

Corela, C., Loureiro, A., Duarte, J. L., Matias, L., Rebelo, T., and Bartolomeu, T. The effect of deep ocean currents on ocean-bottom seismometers records. *Natural Hazards and Earth System Sciences*, 23(4):1433–1451, 2023. doi: 10.5194/nhess-23-1433-2023.

Cranch, G., Nash, P., and Kirkendall, C. Large-scale remotely interrogated arrays of fiber-optic interferometric sensors for underwater acoustic applications. *IEEE Sensors Journal*, 3(1):19–30, February 2003. doi: 10.1109/jsen.2003.810102.

Crawford, W. C., Webb, S. C., and Hildebrand, J. A. Seafloor compliance observed by long-period pressure and displacement measurements. *Journal of Geophysical Research: Solid Earth*, 96 (B10):16151–16160, September 1991. doi: 10.1029/91jb01577.

Crotwell, H. P., Owens, T. J., and Ritsema, J. The TauP Toolkit: Flexible Seismic Travel-time and Ray-path Utilities. *Seismological Research Letters*, 70(2):154–160, March 1999. doi: 10.1785/gssrl.70.2.154.

Cummings, W. C. and Thompson, P. O. Underwater Sounds from the Blue Whale, Balaenoptera musculus. *The Journal of the Acoustical Society of America*, 50(4B):1193–1198, October 1971. doi: 10.1121/1.1912752.

Cuny, T., Bettinelli, P., and Le Calvez, J. Variable gauge length: Processing theory and applications to distributed acoustic sensing. *Geophysical Prospecting*, November 2024. doi: 10.1111/1365-2478.13640.

Daley, T., Miller, D., Dodds, K., Cook, P., and Freifeld, B. Field testing of modular borehole monitoring with simultaneous distributed acoustic sensing and geophone vertical seismic profiles at Citronelle, Alabama. *Geophysical Prospecting*, 64(5):1318–1334, November 2015. doi: 10.1111/1365-2478.12324.

Dean, T., Hartog, A., Papp, B., and Frignet, B. Fibre Optic Based Vibration Sensing: Nature of the Measurement. In *3rd EAGE Workshop on Borehole Geophysics*, Athens2015. EAGE Publications BV, April 2015. doi: 10.3997/2214-4609.201412183.

Dean, T., Cuny, T., and Hartog, A. H. The effect of gauge length on axially incident P-waves measured using fibre optic distributed vibration sensing. *Geophysical Prospecting*, 65(1):184–193, July 2016. doi: 10.1111/1365-2478.12419.

Delarue, J., Todd, S. K., Van Parijs, S. M., and Di Iorio, L. Geographic variation in Northwest Atlantic fin whale (Balaenoptera physalus) song: Implications for stock structure assessment. *The Journal of the Acoustical Society of America*, 125 (3):1774–1782, March 2009. doi: 10.1121/1.3068454.

Dong, L. Stimulated thermal Rayleigh scattering in optical fibers. *Optics Express*, 21(3):2642, January 2013. doi: 10.1364/oe.21.002642.

Douglass, A. S., Abadi, S., and Lipovsky, B. P. Distributed Acoustic Sensing for detecting near surface hydroacoustic signals. *Authorea Preprints*, 2023. doi: 10.1121/10.0019703.

Dunlop, R. A., Noad, M. J., Cato, D. H., and Stokes, D. The social vocalization repertoire of east Australian migrating humpback whales (Megaptera novaeangliae). *The Journal of the Acoustical Society of America*, 122(5):2893–2905, November 2007. doi: 10.1121/1.2783115.

Dunlop, R. A., Cato, D. H., and Noad, M. J. Non-song acoustic communication in migrating humpback whales (Megaptera novaeangliae). *Marine Mammal Science*, 24(3):613–629, July 2008. doi: 10.1111/j.1748-7692.2008.00208.x.

Essing, D., Schlindwein, V., Schmidt-Aursch, M. C., Hadziioannou, C., and Stähler, S. C. Characteristics of Current-Induced Harmonic Tremor Signals in Ocean-Bottom Seismometer Records. *Seismological Research Letters*, apr 2021. doi: 10.1785/0220200397.

Feng, C. *The measurement of vortex induced effects in flow past stationary and oscillating circular and D-section cylinders*. PhD thesis, University of British Columbia, 1968. https://open.library.ubc.ca/soa/cIRcle/collections/ubctheses/831/items/1.0104049.

Fernández-Ruiz, M. R., Soto, M. A., Williams, E. F., Martin-Lopez, S., Zhan, Z., Gonzalez-Herraez, M., and Martins, H. F. Distributed acoustic sensing for seismic activity monitoring. *APL Photonics*, 5(3):030901, March 2020. doi: 10.1063/1.5139602.

Fernandez-Ruiz, M. R., Martins, H. F., Williams, E. F., Becerril, C., Magalhaes, R., Costa, L., Martin-Lopez, S., Jia, Z., Zhan, Z., and Gonzalez-Herraez, M. Seismic Monitoring With Distributed Acoustic Sensing From the Near-Surface to the Deep Oceans. *Journal of Lightwave Technology*, 40(5):1453–1463, March 2022. doi: 10.1109/jlt.2021.3128138.

Flores, D. M., Sladen, A., Ampuero, J.-P., Mercerat, E. D., and Rivet, D. Monitoring Deep Sea Currents With Seafloor Distributed Acoustic Sensing. *Earth and Space Science*, 10(6), 2023. doi: 10.1029/2022ea002723.

Frazão, H., Prien, R., Müller, T., Schulz-Bull, D., and Waniek, J. 30 years of temporal variability of temperature and currents below the main thermocline between 1980?2009 in the subtropical Northeast Atlantic (Kiel 276, 33°N, 22°W).

Journal of Marine Systems, 217:103517, May 2021. doi: 10.1016/j.jmarsys.2021.103517.

Froggatt, M. and Moore, J. High-spatial-resolution distributed strain measurement in optical fiber with Rayleigh scatter. *Applied Optics*, 37(10):1735, April 1998. doi: 10.1364/ao.37.001735.

GA 101058518, 2022. doi: 10.3030/101058518.

GA 101095055, 2023. doi: 10.3030/101095055.

Gabai, H. and Eyal, A. On the sensitivity of distributed acoustic sensing. *Optics Letters*, 41(24):5648, December 2016. doi: 10.1364/ol.41.005648.

GEBCO Compilation Group. GEBCO 2023 Grid, 2023. doi: 10.5285/F98B053B-0CBC-6C23-E053-6C86ABC0AF7B.

González-Herráez, M. Observing ocean waves and their nonlinear interactions using fiber optic cables. In Scheuer, J. and Shahriar, S. M., editors, *Quantum Sensing, Imaging, and Precision Metrology II*, volume 12912, page 129120I. International Society for Optics and Photonics, SPIE, 2024. doi: 10.1117/12.3012361.

Griffin, O. M. *Vortex-induced vibrations of marine cables and structures*. Naval Research Laboratory, 1985.

Gök, R., Walter, W. R., Barno, J., Downie, C., Mellors, R. J., Mayeda, K., Roman-Nieves, J., Templeton, D., and Ajo-Franklin, J. Reliable Earthquake Source Parameters Using Distributed Acoustic Sensing Data Derived from Coda Envelopes. *Seismological Research Letters*, March 2024. doi: 10.1785/0220230270.

Hamza, A., Sokkar, T., EL-Farahaty, K., and EL-Dessouky, H. Influence of temperature on the optical and structural properties along the diameter of optical fibres. *Optics and Lasers in Engineering*, 41(2):261–275, February 2004. doi: 10.1016/s0143-8166(02)00199-9.

Hartog, A. H. *An introduction to distributed optical fibre sensors*. CRC press, 2017. doi: 10.1201/9781315119014.

Hatch, L. T. and Clark, C. W. Acoustic differentiation between fin whales in both the NorthAtlantic and North Pacific Oceans, and integration with genetic estimates of divergence. *Unpublished paper presented to the IWC Scientific Committee*, pages 1–37, 2004.

Helble, T. A., Guazzo, R. A., Alongi, G. C., Martin, C. R., Martin, S. W., and Henderson, E. E. Fin Whale Song Patterns Shift Over Time in the Central North Pacific. *Frontiers in Marine Science*, 7, October 2020. doi: 10.3389/fmars.2020.587110.

Hilmo, R. and Wilcock, W. S. D. Estimating distances to baleen whales using multipath arrivals recorded by individual seafloor seismometers at full ocean depth. *The Journal of the Acoustical Society of America*, 155(2):930–951, 02 2024. doi: 10.1121/10.0024615.

Hocker, G. B. Fiber-optic sensing of pressure and temperature. *Applied Optics*, 18(9):1445, May 1979. doi: 10.1364/ao.18.001445.

Hubbard, P. G., Vantassel, J. P., Cox, B. R., Rector, J. W., Yust, M. B. S., and Soga, K. Quantifying the Surface Strain Field Induced by Active Sources with Distributed Acoustic Sensing: Theory and Practice. *Sensors*, 22(12):4589, June 2022. doi: 10.3390/s22124589.

Ide, S., Araki, E., and Matsumoto, H. Very broadband strain-rate measurements along a submarine fiber-optic cable off Cape Muroto, Nankai subduction zone, Japan. *Earth, Planets and Space*, 73(1), 2021. doi: 10.1186/s40623-021-01385-5.

Janneh, M., Bruno, F., Guardato, S., Donnarumma, G., Iannaccone, G., Gruca, G., Werzinger, S., Gunda, A., Rijnveld, N., Cutolo, A., Pisco, M., and Cusano, A. Field demonstration of an optical fiber hydrophone for seismic monitoring at Campi-Flegrei caldera. *Optics & Laser Technology*, 158:108920, February 2023. doi: 10.1016/j.optlastec.2022.108920.

Johnson, S. C., Širović, A., Buccowich, J. S., Debich, A. J., Roche, L. K., Thayre, B., Wiggins, S. M., Hildebrand, J. A., Hodge, L. E., and Read, A. J. Passive Acoustic Monitoring for Marine Mammals in the Jacksonville Range Complex 2010. Final Report. Submitted to Naval Facilities Engineering Command (NAVFAC) Atlantic, Norfolk, Virginia, under Contract No. N62470-10D-3011 issued to HDR, Inc. Technical report, Scripps Institution of Oceanography, University of California San Diego, 2014.

Juškaitis, R., Mamedov, A. M., Potapov, V. T., and Shatalin, S. V. Interferometry with Rayleigh backscattering in a single-mode optical fiber. *Optics Letters*, 19(3):225, February 1994. doi: 10.1364/ol.19.000225.

Juškaitis, R., Mamedov, A. M., Potapov, V. T., and Shatalin, S. V. Distributed interferometric fiber sensor system. *Optics Letters*, 17 (22):1623, November 1992. doi: 10.1364/ol.17.001623.

Kennett, B. L. N. and Engdahl, E. R. Traveltimes for global earthquake location and phase identification. *Geophysical Journal International*, 105(2):429–465, May 1991. doi: 10.1111/j.1365-246x.1991.tb06724.x.

Kislov, K. V. and Gravirov, V. V. Distributed Acoustic Sensing: A New Tool or a New Paradigm. *Seismic Instruments*, 58(5):485–508, September 2022. doi: 10.3103/s0747923922050085.

Kovachev, S. A., Demidova, T. A., and Son'kin, A. V. Properties of Noise Registered by Pop-Up Ocean-Bottom Seismographs. *Journal of Atmospheric and Oceanic Technology*, 14(4):883–888, aug 1997. doi: 10.1175/1520-0426(1997)014<0883:ponrbp>2.0.co;2.

Kuvshinov, B. Interaction of helically wound fibre-optic cables with plane seismic waves. *Geophysical Prospecting*, 64(3): 671–688, September 2015. doi: 10.1111/1365-2478.12303.

Käse, R. H. and Siedler, G. Meandering of the subtropical front south-east of the Azores. *Nature*, 300(5889):245–246, November 1982. doi: 10.1038/300245a0.

Landrø, M., Bouffaut, L., Kriesell, H. J., Potter, J. R., Rørstadbotnen, R. A., Taweesintananon, K., Johansen, S. E., Brenne, J. K., Haukanes, A., Schjelderup, O., et al. Sensing whales, storms, ships and earthquakes using an Arctic fibre optic cable. *Scientific Reports*, 12(1):19226, 2022. doi: 10.1002/essoar.10507855.1.

LA/P/0068/2020, 2020. doi: 10.54499/LA/P/0068/2020.

Lewis, L. A. and Širović, A. Variability in blue whale acoustic behavior off southern California. *Marine Mammal Science*, 34(2): 311–329, October 2018. doi: 10.1111/mms.12458.

Lindsey, N. J. and Martin, E. R. Fiber-Optic Seismology. *Annual Review of Earth and Planetary Sciences*, 49(1):309–336, May 2021. doi: 10.1146/annurev-earth-072420-065213.

Lindsey, N. J., Martin, E. R., Dreger, D. S., Freifeld, B., Cole, S., James, S. R., Biondi, B. L., and Ajo-Franklin, J. B. Fiber-Optic Network Observations of Earthquake Wavefields. *Geophysical Research Letters*, 44(23), 2017. doi: 10.1002/2017gl075722.

Lindsey, N. J., Dawe, T. C., and Ajo-Franklin, J. B. Illuminating seafloor faults and ocean dynamics with dark fiber distributed acoustic sensing. *Science*, 366(6469):1103–1107, 2019. doi: 10.1126/science.aay5881.

Lindsey, N. J., Rademacher, H., and Ajo-Franklin, J. B. On the Broadband Instrument Response of Fiber-Optic DAS Arrays. *Journal of Geophysical Research: Solid Earth*, 125(2), February 2020. doi: 10.1029/2019jb018145.

Lior, I., Sladen, A., Mercerat, D., Ampuero, J.-P., Rivet, D., and Sambolian, S. Strain to ground motion conversion of distributed acoustic sensing data for earthquake magnitude and stress drop determination. *Solid Earth*, 12(6):1421–1442, June 2021. doi: 10.5194/se-12-1421-2021.

Loureiro, A. DAS dataset from the GeoLab fibre, Madeira, Portugal, 2023. doi: 10.7914/TPN4-MP07.

Loureiro, A. DAS dataset from the GeoLab fibre, Madeira, Portugal, 2024. doi: 10.14470/8K802502.

Martin, E. R., Lindsey, N. J., Ajo-Franklin, J. B., and Biondi, B. L. *Introduction to Interferometry of Fiber-Optic Strain Measurements*, pages 111–129. Wiley, 2021. doi: 10.1002/9781119521808.ch9.

Mateeva, A., Lopez, J., Potters, H., Mestayer, J., Cox, B., Kiyashchenko, D., Wills, P., Grandi, S., Hornman, K., Kuvshinov, B., Berlang, W., Yang, Z., and Detomo, R. Distributed acoustic sensing for reservoir monitoring with vertical seismic profiling. *Geophysical Prospecting*, 62(4):679–692, May 2014. doi: 10.1111/1365-2478.12116.

Matias, L. and Harris, D. A single-station method for the detection, classification and location of fin whale calls using ocean-bottom seismic stations. *The Journal of the Acoustical Society of America*, 138(1):504–520, July 2015. doi: 10.1121/1.4922706.

McDonald, M. A., Mesnick, S. L., and Hildebrand, J. A. Biogeographic characterisation of blue whale song worldwide: using song to identify populations. *Journal of Cetacean Research and Management*, 8(1):55–65, March 2006. doi: 10.47536/jcrm.v8i1.702.

Mellinger, D. K. and Clark, C. W. Blue whale (Balaenoptera musculus) sounds from the North Atlantic. *The Journal of the Acoustical Society of America*, 114(2):1108–1119, July 2003. doi: 10.1121/1.1593066.

Miller, B. S., Miller, B. S., Stafford, K. M., Van Opzeeland, I., Harris, D., Samaran, F., Širović, A., Buchan, S., Findlay, K., Balcazar, N., Nieukirk, S., Leroy, E. C., Aulich, M., Shabangu, F. W., Dziak, R. P., Lee, W. S., and Hong, J. K. An open access dataset for developing automated detectors of Antarctic baleen whale sounds and performance evaluation of two commonly used detectors. *Scientific Reports*, 11(1), January 2021. doi: 10.1038/s41598-020-78995-8.

Miller, B. S., Madhusudhana, S., Aulich, M. G., and Kelly, N. Deep learning algorithm outperforms experienced human observer at detection of blue whale D-calls: a double-observer analysis. *Remote Sensing in Ecology and Conservation*, 9(1):104–116, August 2022. doi: 10.1002/rse2.297.

Miller, B. S., Andrews-Goff, V., Barlow, J., Bell, E., Calderan, S., Double, M. C., Gedamke, J., Kelly, N., Laverick, S., Leaper, R., Miller, E. J., Reeve, K., Širović, A., and Stafford, K. M. Antarctic sonobuoy surveys for blue whales from 2006-2021 reveal contemporary distribution, changes over time, and paths to further our understanding of their distribution and biology. *Frontiers in Marine Science*, 11, 2024. doi: 10.3389/fmars.2024.1324816.

MODAS project 2022.02359.PTDC. Monitoring the Oceans with Distributed Acoustic Sensing, 2022. doi: 10.54499/2022.02359.PTDC.

Nieukirk, S. L., Mellinger, D. K., Dziak, R. P., Matsumoto, H., and Klinck, H. Multi-year occurrence of sei whale calls in North Atlantic polar waters. *The Journal of the Acoustical Society of America*, 147(3):1842–1850, March 2020. doi: 10.1121/10.0000931.

Notarbartolo-di Sciara, G., Zanardell, M., Jahoda, M., Panigada, S., and Airoldi, S. The fin whale Balaenoptera physalus (L. 1758) in the Mediterranean Sea. *Mammal Review*, 33(2):105–150, May 2003. doi: 10.1046/j.1365-2907.2003.00005.x.

Oleson, E., Calambokidis, J., Burgess, W., McDonald, M., LeDuc, C., and Hildebrand, J. Behavioral context of call production by eastern North Pacific blue whales. *Marine Ecology Progress Series*, 330:269–284, January 2007. doi: 10.3354/meps330269.

Paitz, P., Edme, P., Gräff, D., Walter, F., Doetsch, J., Chalari, A., Schmelzbach, C., and Fichtner, A. Empirical Investigations of the Instrument Response for Distributed Acoustic Sensing (DAS) across 17 Octaves. *Bulletin of the Seismological Society of America*, 111(1):1–10, October 2020. doi: 10.1785/0120200185.

Palmieri, L. Distributed Optical Fiber Sensing Based on Rayleigh Scattering. *The Open Optics Journal*, 7(1):104–127, 2013. doi: 10.2174/1874328501307010104.

Papp, B., Donno, D., Martin, J. E., and Hartog, A. H. A study of the geophysical response of distributed fibre optic acoustic sensors through laboratory-scale experiments. *Geophysical Prospecting*, 65(5):1186–1204, November 2016. doi: 10.1111/1365-2478.12471.

Payne, R. and Webb, D. Orientation by means of long range acoustic signaling in baleen whales. *Annals of the New York Academy of Sciences*, 188(1):110–141, 1971. doi: 10.1111/j.1749-6632.1971.tb13093.x.

Peláez Quiñones, J. D., Sladen, A., Ponte, A., Lior, I., Ampuero, J.-P., Rivet, D., Meulé, S., Bouchette, F., Pairaud, I., and Coyle, P. High resolution seafloor thermometry for internal wave and upwelling monitoring using Distributed Acoustic Sensing. *Scientific Reports*, 13(1), October 2023. doi: 10.1038/s41598-023-44635-0.

Pereira, A., Harris, D., Tyack, P., and Matias, L. Fin whale acoustic presence and song characteristics in seas to the southwest of Portugal. *The Journal of the Acoustical Society of America*, 147 (4):2235–2249, apr 2020a. doi: 10.1121/10.0001066.

Pereira, A., Harris, D., Tyack, P., and Matias, L. On the use of the Lloyd's Mirror effect to infer the depth of vocalizing fin whales. *The Journal of the Acoustical Society of America*, 148(5): 3086–3101, 2020b. doi: 10.1121/10.0002426.

Potter, J. R., Potter, J. R., Wengle, E., Dong, H., Trondheim, N., and Rørstadbotnen, R. A. Distributed Acoustic Sensing of Underwater Acoustic Communication Packets: Effects of Frequency and Incidence Angle. *[preprint]*, October 2024. doi: 10.22541/essoar.173031738.81849568/v1.

Prieto, R., Silva, M., Waring, G., and Gonçalves, J. Sei whale movements and behaviour in the North Atlantic inferred from satellite telemetry. *Endangered Species Research*, 26(2):103–113, December 2014. doi: 10.3354/esr00630.

Rathod, R., Pechstedt, R. D., Jackson, D. A., and Webb, D. J. Distributed temperature-change sensor based on Rayleigh backscattering in an optical fiber. *Optics Letters*, 19(8):593, April 1994. doi: 10.1364/ol.19.000593.

Rice, A. N., Palmer, K. J., Tielens, J. T., Muirhead, C. A., and Clark, C. W. Potential Bryde's whale (Balaenoptera edeni) calls recorded in the northern Gulf of Mexico. *The Journal of the Acoustical Society of America*, 135(5):3066–3076, May 2014. doi: 10.1121/1.4870057.

Rivet, D., de Cacqueray, B., Sladen, A., Roques, A., and Calbris, G. Preliminary assessment of ship detection and trajectory evaluation using distributed acoustic sensing on an optical fiber telecom cable. *The Journal of the Acoustical Society of America*, 149 (4):2615–2627, April 2021. doi: 10.1121/10.0004129.

Romagosa, M., Boisseau, O., Cucknell, A.-C., Moscrop, A., and McLanaghan, R. Source level estimates for sei whale (Balaenoptera borealis) vocalizations off the Azores. *The Journal of the Acoustical Society of America*, 138(4):2367–2372, October 2015. doi: 10.1121/1.4930900.

Romagosa, M., Baumgartner, M., Cascão, I., Lammers, M. O., Marques, T. A., Santos, R. S., and Silva, M. A. Baleen whale acoustic presence and behaviour at a Mid-Atlantic migratory habitat, the Azores Archipelago. *Scientific Reports*, 10(1), 2020. doi: 10.1038/s41598-020-61849-8.

Seabrook, B. C., Ellmauthaler, A., LeBlanc, M., Jaaskelainen, M., Maida, J. L., and Wilson, G. A. Comparison of Raman, Brillouin, and Rayleigh Distributed Temperature Measurements in

High-Rate Wells. *Petrophysics – The SPWLA Journal of Formation Evaluation and Reservoir Description*, 63(6):685–699, December 2022. doi: 10.30632/pjv63n6-2022a8.

Siedler, G., Armi, L., and Müller, T. J. Meddies and decadal changes at the Azores Front from 1980 to 2000. *Deep Sea Research Part II: Topical Studies in Oceanography*, 52(3–4):583–604, February 2005. doi: 10.1016/j.dsr2.2004.12.010.

Silva, M. A., Prieto, R., Jonsen, I., Baumgartner, M. F., and Santos, R. S. North Atlantic Blue and Fin Whales Suspend Their Spring Migration to Forage in Middle Latitudes: Building up Energy Reserves for the Journey? *PLoS ONE*, 8(10):e76507, October 2013. doi: 10.1371/journal.pone.0076507.

Sinnett, G., Davis, K. A., Lucas, A. J., Giddings, S. N., Reid, E., Harvey, M. E., and Stokes, I. Distributed Temperature Sensing for Oceanographic Applications. *Journal of Atmospheric and Oceanic Technology*, 37(11):1987–1997, November 2020. doi: 10.1175/jtech-d-20-0066.1.

Širović, A., Hildebrand, J. A., and Wiggins, S. M. Blue and fin whale call source levels and propagation range in the Southern Ocean. *The Journal of the Acoustical Society of America*, 122(2): 1208–1215, August 2007. doi: 10.1121/1.2749452.

Skop, R. and Griffin, O. On a theory for the vortex-excited oscillations of flexible cylindrical structures. *Journal of Sound and Vibration*, 41(3):263–274, August 1975. doi: 10.1016/s0022-460x(75)80173-8.

Sladen, A., Rivet, D., Ampuero, J. P., De Barros, L., Hello, Y., Calbris, G., and Lamare, P. Distributed sensing of earthquakes and ocean-solid Earth interactions on seafloor telecom cables. *Nature Communications*, 10(1), December 2019. doi: 10.1038/s41467-019-13793-z.

Spingys, C. P., Naveira Garabato, A. C., and Belal, M. Distributed Optical Fibre Sensing for High Space-Time Resolution Ocean Velocity Observations: A Case Study From a Macrotidal Channel. *Earth and Space Science*, 11(5), May 2024. doi: 10.1029/2023ea003315.

Stimpert, A. K., Au, W. W., Parks, S. E., Hurst, T., and Wiley, D. N. Common humpback whale (Megaptera novaeangliae) sound types for passive acoustic monitoring. *The Journal of the Acoustical Society of America*, 129(1):476–482, 2011. doi: 10.1121/1.3504708.

Stähler, S. C., Schmidt-Aursch, M. C., Hein, G., and Mars, R. A Self-Noise Model for the German DEPAS OBS Pool. *Seismological Research Letters*, 89(5):1838–1845, 2018. doi: 10.1785/0220180056.

Sun, J., Wang, Y., Zhang, J., Liang, Y., Zhang, G., Wan, A., Zhang, S., Ye, Z., Zhou, Y., Jing, Q., Rao, Y., Wang, H., and Wang, Z. 2-D Phase Unwrapping in DAS Based on Transport-of-Intensity-Equation: Principle, Algorithm and Field Test. *Journal of Lightwave Technology*, pages 1–11, 2024. doi: 10.1109/jlt.2024.3391275.

Toulouse, J. Optical nonlinearities in fibers: review, recent examples, and systems applications. *Journal of Lightwave Technology*, 23(11):3625–3641, November 2005. doi: 10.1109/jlt.2005.855877.

Trabattoni, A., Biagioli, F., Strumia, C., van den Ende, M., di Uccio, F. S., Festa, G., Rivet, D., Sladen, A., Ampuero, J. P., Métaxian, J.-P., and Stutzmann, É. From strain to displacement: using deformation to enhance distributed acoustic sensing applications. *Geophysical Journal International*, 235(3):2372–2384, 2023. doi: 10.1093/gji/ggad365.

Triantafyllou, M. S., Bourguet, R., Dahl, J., and Modarres-Sadeghi, Y. *Vortex-Induced Vibrations*, pages 819–850. Springer International Publishing, 2016. doi: 10.1007/978-3-319-16649-0_36.

Ugalde, A., Becerril, C., Villaseñor, A., Ranero, C. R., Fernández-Ruiz, M. R., Martin-Lopez, S., González-Herráez, M., and Martins, H. F. Noise Levels and Signals Observed on Submarine Fibers in the Canary Islands Using DAS. *JASA Express Letters*, 93(1): 351–363, 2021. doi: 10.1785/0220210049.

UID/PRR/50019/2025, 2025. doi: 10.54499/UID/PRR/50019/2025.

Valente, R., Correia, A. M., Gil, A., González García, L., and Sousa-Pinto, I. Baleen whales in Macaronesia: occurrence patterns revealed through a bibliographic review. *Mammal Review*, 49(2): 129–151, February 2019. doi: 10.1111/mam.12148.

van den Ende, M., Trabattoni, A., Baillet, M., and Rivet, D. An analysis of the dynamic range of Distributed Acoustic Sensing for Earthquake Early Warning. *Earth ArXiv [pre-print]*, April 2024. doi: 10.31223/x5kh5r.

van den Ende, M. P. A. and Ampuero, J.-P. Evaluating seismic beamforming capabilities of distributed acoustic sensing arrays. *Solid Earth*, 12(4):915–934, 2021. doi: 10.5194/se-12-915-2021.

Vidal-Moreno, P. J., Rochat, E., Fermoso, P., Fernández-Ruiz, M. R., Martins, H., Martin-Lopez, S., Ocaña, M., and Gonzalez-Herraez, M. Cancellation of reference update-induced 1/f noise in a chirped-pulse DAS. *Optics Letters*, 47(14):3588, July 2022. doi: 10.1364/ol.465367.

Waagaard, O. H., Rønnekleiv, E., Haukanes, A., Stabo-Eeg, F., Thingbø, D., Forbord, S., Aasen, S. E., and Brenne, J. K. Real-time low noise distributed acoustic sensing in 171 km low loss fiber. *OSA Continuum*, 4(2):688, February 2021. doi: 10.1364/osac.408761.

Watkins, W. A. Activities and underwater sounds of fin whales. *Sci. Rep. Whales Res. Inst*, 33:83–117, 1981. doi: 10.1016/0198-0254(82)90294-1.

Watkins, W. A., Tyack, P., Moore, K. E., and Bird, J. E. The 20-Hz signals of finback whales (Balaenoptera-physalus). *The Journal of the Acoustical Society of America*, 82(6):1901–1912, December 1987. doi: 10.1121/1.395685.

Wenzel, F. W., Broms, F., López-Suárez, P., Lopes, K., Veiga, N., Yeoman, K., Rodrigues, M. S. D., Allen, J., Fernald, T. W., Stevick, P. T., Jones, L., Jann, B., Bouveret, L., Ryan, C., Berrow, S., and Corkeron, P. Humpback Whales (Megaptera novaeangliae) in the Cape Verde Islands: Migratory Patterns, Resightings, and Abundance. *Aquatic Mammals*, 46(1):21–31, January 2020. doi: 10.1578/am.46.1.2020.21.

Wessel, P., Luis, J. F., Uieda, L., Scharroo, R., Wobbe, F., Smith, W. H. F., and Tian, D. The Generic Mapping Tools Version 6. *Geochemistry, Geophysics, Geosystems*, 20(11):5556–5564, 2019. doi: 10.1029/2019gc008515.

Wiggins, S. M., Oleson, E. M., McDonald, M. A., and Hildebrand, J. A. Blue Whale (Balaenoptera musculus) Diel Call Patterns Offshore of Southern California. *Aquatic Mammals*, 31(2):161–168, September 2005. doi: 10.1578/am.31.2.2005.161.

Wilcock, W. S. D., Abadi, S., and Lipovsky, B. P. Distributed acoustic sensing recordings of low-frequency whale calls and ship noise offshore Central Oregon. *JASA Express Letters*, 3(2), 2023. doi: 10.1121/10.0017104.

Williams, E. F., Fernández-Ruiz, M. R., Magalhaes, R., Vanthillo, R., Zhan, Z., González-Herráez, M., and Martins, H. F. Distributed sensing of microseisms and teleseisms with submarine dark fibers. *Nature Communications*, 10(1), December 2019. doi: 10.1038/s41467-019-13262-7.

Williams, E. F., Zhan, Z., Martins, H. F., Fernández-Ruiz, M. R., Martín-López, S., González-Herráez, M., and Callies, J. Surface Gravity Wave Interferometry and Ocean Current Monitoring With Ocean-Bottom DAS. *Journal of Geophysical Research: Oceans*, 127(5), 2022. doi: 10.1029/2021jc018375.

Williams, E. F., Ugalde, A., Martins, H. F., Becerril, C. E., Callies, J.,

Claret, M., Fernandez-Ruiz, M. R., Gonzalez-Herraez, M., Martin-Lopez, S., Pelegri, J. L., Winters, K. B., and Zhan, Z. Fiber-Optic Observations of Internal Waves and Tides. *Journal of Geophysical Research: Oceans*, 128(9), 2023. doi: 10.1029/2023jc019980.

Xiao, H., Zhang, S., Moss, R., and Zhan, Z. Imaging Underwater Faults and Tracking Whales with Optical Fiber Sensing. *Seismological Research Letters*, January 2025. doi: 10.1785/0220240359.

Yang, Y., Atterholt, J. W., Shen, Z., Muir, J. B., Williams, E. F., and Zhan, Z. Sub-Kilometer Correlation Between Near-Surface Structure and Ground Motion Measured With Distributed Acoustic Sensing. *Geophysical Research Letters*, 49(1), December 2021. doi: 10.1029/2021gl096503.

Yeung, W. F. and Johnston, A. R. Effect of temperature on optical fiber transmission. *Applied Optics*, 17(23):3703, December 1978. doi: 10.1364/ao.17.003703.

Zhai, Q., Yin, J., Yang, Y., Atterholt, J. W., Li, J., Husker, A., and Zhan, Z. Comprehensive Evaluation of DAS Amplitude and Its Implications for Earthquake Early Warning and Seismic Interferometry. *Journal of Geophysical Research: Solid Earth*, 130(4), March 2025. doi: 10.1029/2024jb030288.

Zhu, W., Mousavi, S. M., and Beroza, G. C. Seismic Signal Denoising and Decomposition Using Deep Neural Networks. *IEEE Transactions on Geoscience and Remote Sensing*, 57(11):9476–9488, November 2019. doi: 10.1109/tgrs.2019.2926772.

Zumberge, M. A., Hatfield, W., and Wyatt, F. K. Measuring Seafloor Strain With an Optical Fiber Interferometer. *Earth and Space Science*, 5(8):371–379, August 2018. doi: 10.1029/2018ea000418.